

A Novel Layer 4 Corticofugal Cell Type/Projection Involved in Thalamo-Cortico-Striatal Sensory Processing

Alice Bertero, Lucia Verrillo, and Alfonso junior Apicella

Department of Biology, Neurosciences Institute, University of Texas at San Antonio, San Antonio, Texas 78249

In sensory cortices, the information flow has been thought to be processed vertically across cortical layers, with layer 4 being the major thalamo-recipient which relays thalamic signals to layer 2/3, which in turn transmits thalamic information to layer 5 and 6 to then leave the cortex to reach subcortical and cortical long-range structures. Although several exceptions to this model have been described, neurons in layer 4 are still considered to establish only local (i.e., interlaminar and short-range) connections. Here, taking advantage of anatomic, electrophysiological, and optogenetic techniques, we describe, for the first time, a long-range corticostriatal class of pyramidal neurons in layer 4 (CS-L4) of the mouse auditory cortex that receive direct thalamic inputs. The CS-L4 neurons are embedded in a feedforward inhibitory circuit involving local parvalbumin neurons and establish connections in the posterior striatum in yet another feedforward inhibitory thalamo→cortico(L4)→striatal circuit which potentially contributes in controlling control the output of striatal spiny projection neurons.

Key words: auditory cortex; corticofugal; GABAergic; glutamatergic; layer 4; parvalbumin-expressing

Significance Statement

The assumption has been that layer 4 neurons are the main thalamic recipient layer, projecting to the upper cortical layer 2/3. However, no study has revealed a detailed understanding of the circuit mechanisms by which layer 4 sends a projection to a subcortical structure, such as the striatum, and differentially innervate the spiny projection neurons (SPNs) and intrastriatal parvalbumin-expressing neurons. For the first time, our results demonstrate that the auditory cortex projects to the posterior part of the dorsal striatum via pyramidal neurons located in layer 4 (CS-L4 neurons). Here we propose a new wiring diagram that implemented the old one, in which layer 4 is not only involved in the transfer of thalamic input to the upper layer 2/3, but can also exert a direct top-down control, bypassing intracortical processing of subcortical structures, such as the posterior part of the dorsal striatum. This poses a new conceptual cell element (CS-L4 neurons) for experimental and theoretical work of the cortical function.

Introduction

The mammalian sensory neocortex, including the auditory cortex (AC), is organized as a six-layer structure. It has been generally assumed that cortical processing is hierarchical, with the anatomic organization providing a defined substrate for precise levels of the transfer of inputs between each layer of the cortex. In this stereotypical architecture, the first cortical processing level for sensory signals happens in layer 4 (L4), the primary recipient of the sensory inputs coming from the thalamus. Since Gilbert & Wiesel's (Gilbert and Wiesel, 1979, 1983) circuit diagram, experiments and theories have suggested that L4 pyramidal neurons project preferentially to superficial layers 2/3 (L2/L3), providing

a canonical intracortical flow of the thalamic input before it is communicated to the rest of the brain (auditory thalamus [medial geniculate body, MGB]→L4→L2/3→layer 5 [L5]→) (Linden and Schreiner, 2003; Winkowski and Kanold, 2013). Therefore, understanding the L4 cell-type composition and connectivity patterns is fundamental to determine its role in the routing of sensory processing arriving from the thalamus.

One of the essential functions of the nervous system is to integrate sensory information to produce an appropriate motor output (Schultz et al., 1997; Haber, 2008). The integration of all the sensory information arriving from the cortex and thalamus is performed in the striatum, the primary structure of the basal ganglia (Flaherty and Graybiel, 1993; Doig et al., 2010; Chen et al., 2019; Ponvert and Jaramillo, 2019). Li et al. (2021) recently revealed that the AC, via L5 pyramidal neurons, and the tail of the dorsal striatum control defensive behavior in mice induced by auditory looming sounds. These results highlighted the importance of the striatum, as the key structure of the basal ganglia, already implicated in various functions, including motor learning, planning, execution, and decision-making (Graybiel et al., 1994; Znamenskiy and Zador, 2013; Graybiel and Grafton, 2015; Xiong

Received Aug. 26, 2021; revised Oct. 11, 2021; accepted Dec. 14, 2021.

Author contributions: A.j.A. designed research; A.j.A., A.B., and L.V. performed research; A.j.A. and A.B. analyzed data; A.j.A. wrote the paper; A.B. wrote the first draft of the paper.

A.j.A. was supported by National Institutes of Health Grants GM122645 and MH123260. We thank Charles Garcia for help with confocal imaging and 3D reconstructions.

The authors declare no competing financial interests.

Correspondence should be addressed to Alfonso junior Apicella at alfonso.apicella@utsa.edu.

<https://doi.org/10.1523/JNEUROSCI.1738-21.2021>

Copyright © 2022 the authors

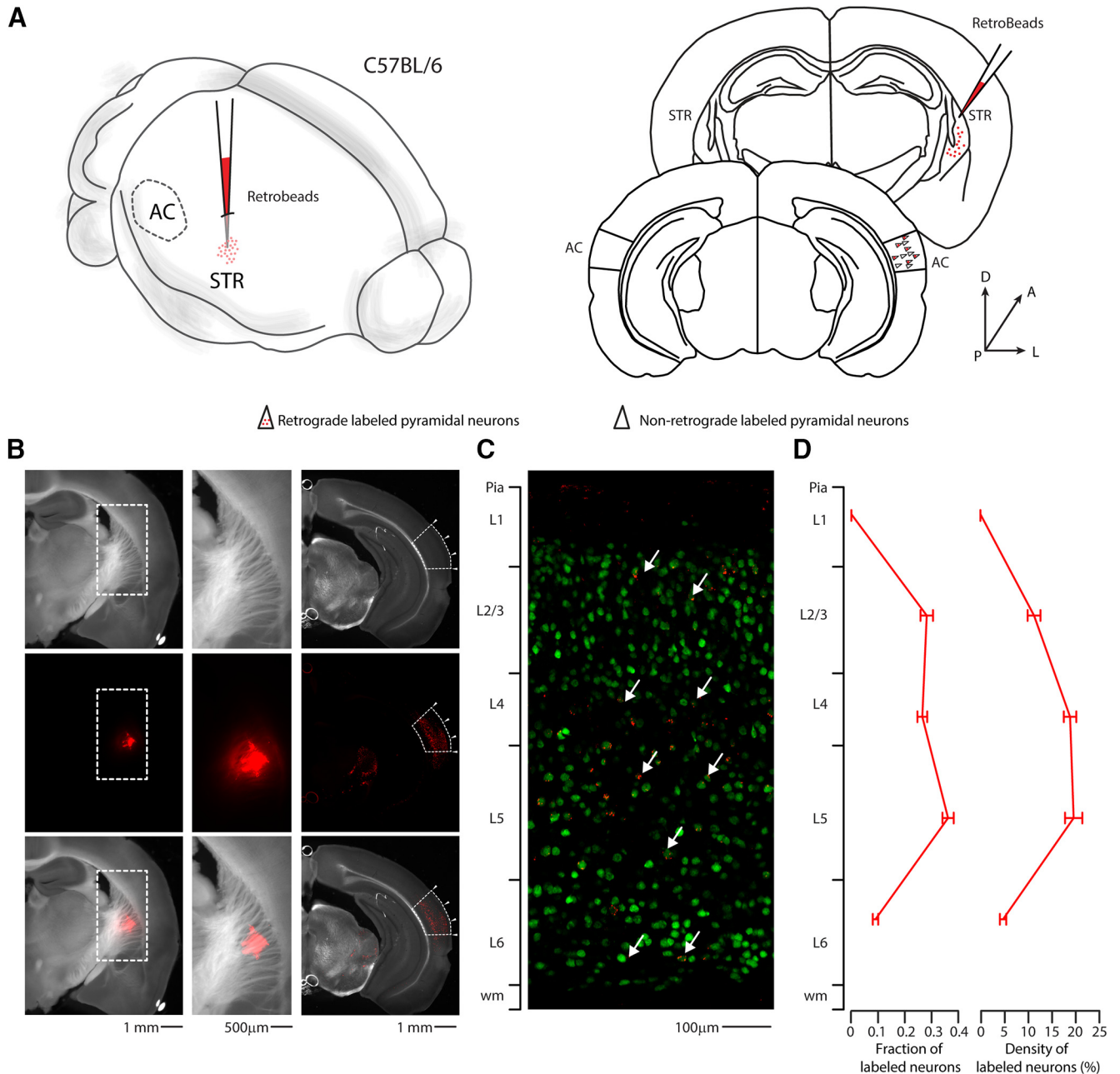


Figure 1. Retrograde quantification of corticostriatal neurons in the AC. **A**, Left, Schematic of the injection site in 3D. Right, Schematic of the Allen Brain Atlas tables and coordinates used for injections and imaging; 30 nl of red RBs was injected in the right striatum, while imaging was performed on the ipsilateral AC of C57BL/6 mice. **B**, Left panels, Top to bottom, Bright field, red fluorescence, and overlay images of the slice containing the injection site for red RBs. Scale bar, 1 mm. Middle panels, Top to bottom, Bright field, red fluorescence, and overlay images of the injected right striatum, corresponding to the dotted boxes in the left panels. Scale bar, 500 μ m. Right panels, Top to bottom, Bright field, red fluorescence, and overlay images of the slice containing the right AC. Dotted boxes indicate the boundaries of the AC, according to the Allen Brain Atlas. Arrowheads indicate the boundaries of the three subdivisions of the AC (dorsal, primary, ventral). Scale bar, 1 mm. **C**, Representative high-resolution confocal image of primary AC, with layer references on the left bar. Green represents NeuN staining. Red represents red RBs. Arrows point at double-labeled neurons, which can be found in every layer except for L1. Scale bar, 100 μ m. **D**, Summary plot indicating the fraction of labeled neurons (left) or the density of double-labeled neurons (right) found in each layer of the whole AC (including dorsal, primary, and ventral) as defined by the Allen Brain Atlas.

et al., 2015), to also be important for defensive behavior (Li et al., 2021). However, the underlying corticostriatal circuits involved in auditory-driven threatening behavior are still unknown.

It is very well established that the corticostriatal input (Guo et al., 2015) primarily originates in the L5 of the cortex and is divided into pathways: the intra-telencephalic (IT-type) pyramidal neurons that project to the ipsilateral and contralateral striatum; and the pyramidal tract and/or projecting (PT-type) pyramidal neurons that send their axons to the downstream areas, such as the thalamus and brainstem with collaterals in the ipsilateral

striatum (Landry et al., 1984; Wilson, 1987; Cowan and Wilson, 1994; Lei et al., 2004; Kress et al., 2013). Furthermore, a growing body of studies have shown the roles that cortical IT- and PT-type neurons have onto different striatal neurons and how these cortical excitatory inputs are the main driving force of the underlying circuit operation performed by the striatum (Tepper et al., 2007). However, the existence and the impact of L4 pyramidal neurons onto striatal neurons have not been described yet. For the first time, our data assign a new corticofugal function to L4 that has been a priority of L5 of the neocortex (for review, see Shepherd, 2013).

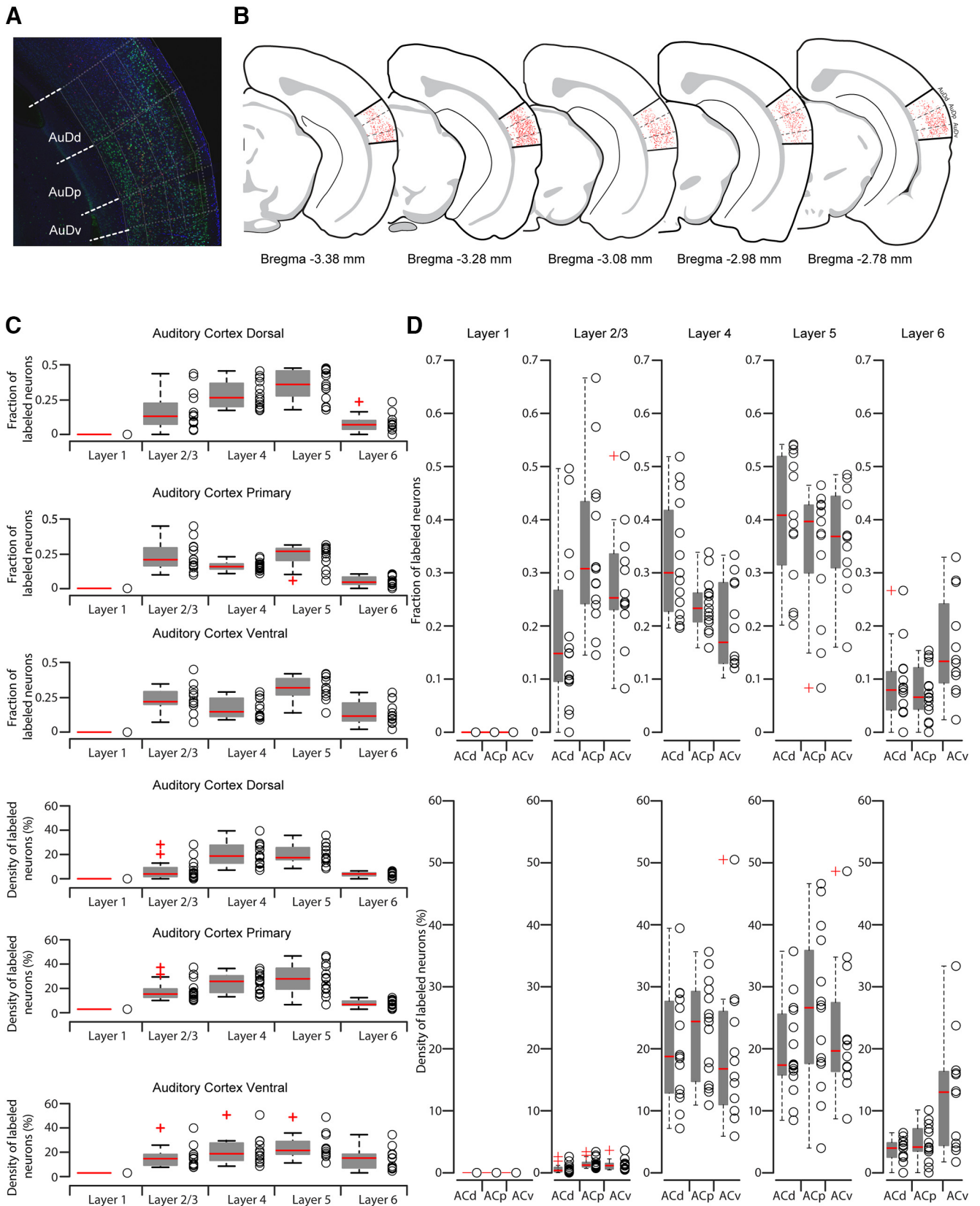


Figure 2. Detailed retrograde quantification of corticostriatal neurons in the AC. **A**, Representative image of NeuN (green), DAPI (blue), and red RB (red) staining of dorsal (AuDd), primary (AuDp), and ventral (AuDv) AC. The grid with normalized distance from pia is superimposed in white and was used to determine the layer distribution of NeuN⁺ and/or red RB⁺ neurons. L1 boundaries were adjusted based on DAPI staining (dashed white line). **B**, Allen Brain Atlas coronal schematics at different anteroposterior levels showing a representative distribution of NeuN/red RBs double-positive neurons in the AC. **C**, Quantification of fraction or density of double-labeled neurons in the three AC subdivisions. Box plots represent median value and distribution. **D**, Quantification of fraction or density of double-labeled neurons in each layer. Box plots represent median value and distribution.

Table 1. Quantification of fraction or density of double-labeled neurons in each layer of the three AC subdivisions

Fraction	L1			L2/L3			L4			L5			L6		
	ACd	ACp	ACv	ACd	ACp	ACv	ACd	ACp	ACv	ACd	ACp	ACv	ACd	ACp	ACv
	0	0	0	0.0950	0.2230	0.2220	0.2860	0.2620	0.3330	0.5000	0.4270	0.3700	0.1190	0.0870	0.0740
	0	0	0	0.1071	0.6667	0.3214	0.4643	0.2333	0.1429	0.3750	0.0833	0.4286	0.0536	0.0167	0.1071
	0	0	0	0.0333	0.3109	0.2424	0.2000	0.2185	0.1364	0.5000	0.4286	0.4849	0.2667	0.0420	0.1364
	0	0	0	0.0000	0.2400	0.3490	0.3330	0.2600	0.2220	0.4810	0.4270	0.3490	0.1850	0.0730	0.0790
	0	0	0	0.1482	0.5745	0.0824	0.5185	0.2766	0.1294	0.2963	0.1489	0.4588	0.0370	0.0000	0.3294
	0	0	0	0.4961	0.3103	0.2610	0.2636	0.2069	0.1300	0.2016	0.3966	0.4780	0.0388	0.0862	0.1300
	0	0	0	0.1490	0.2800	0.5200	0.2450	0.3230	0.1200	0.5320	0.3330	0.1600	0.0740	0.0650	0.2000
	0	0	0	0.4750	0.4423	0.3051	0.3000	0.2115	0.2825	0.2250	0.1923	0.2994	0.0000	0.1539	0.1130
	0	0	0	0.1587	0.4074	0.4000	0.2222	0.2444	0.3060	0.5397	0.2889	0.2710	0.0794	0.0593	0.0240
	0	0	0	0.1000	0.2800	0.2400	0.3750	0.2560	0.2800	0.5250	0.4150	0.3200	0.0000	0.0490	0.1600
	0	0	0	0.0980	0.1690	0.2449	0.4314	0.2254	0.1020	0.3726	0.4648	0.3674	0.0980	0.1409	0.2857
	0	0	0	0.3365	0.2500	0.0226	0.1963	0.1912	0.0290	0.3925	0.4265	0.0548	0.0748	0.1324	0.0419
	0	0	-	0.2960	0.4490	-	0.2110	0.1590	-	0.4080	0.3740	-	0.0850	0.0190	-
	0	0	-	0.1800	0.1452	-	0.4800	0.3387	-	0.2200	0.3710	-	0.1200	0.1452	-
	0	0	-	0.0417	0.3077	-	0.3333	0.1868	-	0.5417	0.4396	-	0.0833	0.0659	-
Minimum	0	0	0	0.0000	0.0192	0.0167	0.0141	0.0182	0.0093	0.0193	0.0086	0.0205	0.0000	0.0000	0.0037
25% Percentile	0	0	0	0.0069	0.0380	0.0206	0.0258	0.0270	0.0156	0.0352	0.0397	0.0359	0.0052	0.0047	0.0096
Median	0	0	0	0.0129	0.0444	0.0352	0.0349	0.0346	0.0294	0.0419	0.0635	0.0480	0.0107	0.0116	0.0232
75% Percentile	0	0	0	0.0405	0.0687	0.0627	0.0448	0.0518	0.0362	0.0611	0.0823	0.0835	0.0128	0.0217	0.0412
Maximum	0	0	0	0.0901	0.1160	0.1137	0.0549	0.0696	0.1053	0.0765	0.1194	0.1255	0.0242	0.0260	0.0668
density	ACd	ACp	ACv	ACd	ACp	ACv	ACd	ACp	ACv	ACd	ACp	ACv	ACd	ACp	ACv
	0%	0%	0%	3.77%	10.41%	4.92%	17.39%	28.13%	18.00%	26.25%	45.36%	14.49%	5.88%	9.89%	3.64%
	0%	0%	0%	2.52%	18.60%	7.09%	27.96%	13.59%	10.00%	17.36%	3.97%	18.75%	2.52%	0.82%	33.33%
	0%	0%	0%	0.90%	28.24%	24.24%	7.14%	30.95%	24.32%	17.24%	39.84%	34.78%	6.45%	4.46%	16.07%
	0%	0%	0%	4.52%	11.92%	12.15%	29.03%	23.15%	19.44%	16.46%	30.83%	21.36%	5.15%	4.40%	4.72%
	0%	0%	0%	28.19%	14.59%	6.48%	39.44%	16.88%	14.47%	13.33%	10.77%	33.33%	1.71%	0.00%	23.73%
	0%	0%	0%	6.80%	30.51%	5.17%	26.56%	35.64%	5.88%	15.57%	46.62%	15.71%	2.78%	10.27%	4.11%
	0%	0%	0%	9.95%	10.66%	16.25%	19.01%	24.39%	12.00%	35.71%	21.38%	8.70%	3.98%	3.73%	13.16%
	0%	0%	0%	3.94%	15.13%	39.13%	18.46%	25.58%	50.51%	9.78%	13.89%	48.62%	0.00%	14.04%	16.53%
	0%	0%	0%	1.65%	36.67%	15.96%	9.40%	33.67%	27.66%	20.73%	37.50%	20.54%	2.56%	6.78%	1.74%
	0%	0%	0%	3.76%	7.67%	12.77%	12.71%	13.04%	28.00%	17.50%	17.89%	17.02%	0.00%	2.08%	5.88%
	0%	0%	0%	20.22%	9.02%	14.29%	28.95%	25.00%	8.77%	23.46%	26.61%	17.14%	4.46%	7.41%	12.84%
	0%	0%	-	12.88%	12.88%	8.05%	18.75%	17.81%	15.52%	29.58%	27.62%	21.52%	4.35%	10.11%	15.85%
	0%	0%	-	4.95%	13.26%	-	13.39%	10.90%	-	26.61%	18.52%	-	4.92%	1.10%	-
	0%	0%	-	1.20%	8.49%	-	23.76%	29.58%	-	8.46%	17.56%	-	4.48%	5.81%	-
	-	0%	-	-	14.00%	-	12.12%	14.05%	-	16.77%	27.03%	-	2.52%	3.95%	-
Minimum	0%	0%	0%	0.90%	7.67%	4.92%	7.14%	10.90%	5.88%	8.46%	3.97%	8.70%	0%	0%	1.74%
25% Percentile	0%	0%	0%	2.30%	10.41%	6.63%	12.71%	14.05%	10.50%	15.57%	17.56%	16.04%	2.52%	2.08%	4.26%
Median	0%	0%	0%	4.23%	13.26%	12.46%	18.75%	24.39%	16.76%	17.36%	26.61%	19.65%	3.98%	4.46%	13%
75% Percentile	0%	0%	0%	10.68%	18.60%	16.18%	27.96%	29.58%	26.83%	26.25%	37.50%	30.38%	4.92%	9.89%	16.42%
Maximum	0%	0%	0%	28.19%	36.67%	39.13%	39.44%	35.64%	50.51%	35.71%	46.62%	48.62%	6.45%	14.04%	33.33%

The present study focused on four main goals: (1) to determine whether L4 pyramidal neurons send long-range projections to the ipsilateral striatum; (2) to describe the anatomic and electrophysiological properties of these L4 corticostriatal pyramidal neurons (CS-L4 pyramidal neurons); (3) to investigate the thalamic inputs onto CS-L4 pyramidal neurons and parvalbumin (Parv) neurons; and (4) to determine the long-range (ipsilateral) excitatory connectivity pattern of CS-L4 pyramidal neurons onto striatal neurons. Our approach consisted of anatomic, optogenetics, and whole-cell patch-clamp methods to investigate these questions.

Using these manipulations, we found that L4 corticostriatal projecting neurons are involved in two distinct thalamocortical and corticostriatal feedforward inhibitory circuits, attributing a specific function to L4 cortical long-range pyramidal neurons in thalamo→cortico(L4)→striatal communication.

Materials and Methods

Animals. All animal procedures were approved by the Institutional Animal Care and Use Committee at the University of Texas at San

Antonio. Procedures followed animal welfare guidelines set by the National Institutes of Health. Mice used in this experiment were housed in a vivarium maintaining a 12 h light/dark schedule and given *ad libitum* access to mouse chow and water.

The following mouse lines were used in this study:

C57BL/6: WT mice [Charles River, 027];

Scnn1a-Cre: B6;C3-Tg(Scnn1a-cre)3Aibs/J [The Jackson Laboratory, stock #009613];

Rosa-tdTomato reporter: B6.CG.Gt(Rosa)26Sortm14(CAG-tdTomato)Hze/J [The Jackson Laboratory, stock #007914];

G42: CB6-Tg(Gad1-EGFP)G42Zjh/J [The Jackson Laboratory, stock #007677];

Parv-Cre: B6.129P2-Pvalbtm1(cre)Arbr/J [The Jackson Laboratory, stock #017320];

Scnn1a-Cre heterozygous mice were crossed with Rosa-tdTomato homozygous reporter mice to generate Scnn1-Cre/TdTomato transgenic line in which L4 cells express the fluorescent reporter tdTomato.

Viral vectors. AAV-flex-Cheta1C-YFP, titer 2.8×10^{12} GC/ml (pAAV-Ef1a-DIO.hChr2(E123T/T159C)-eYFP, Addgene viral prep #35509-AAV9);

AAV-flex-Halo-YFP, titer 3.1×10^{12} GC/ml (pAAV-Ef1a-DIO.eNpHR.3.0-eYFP, Addgene viral prep #26966-AAV1);

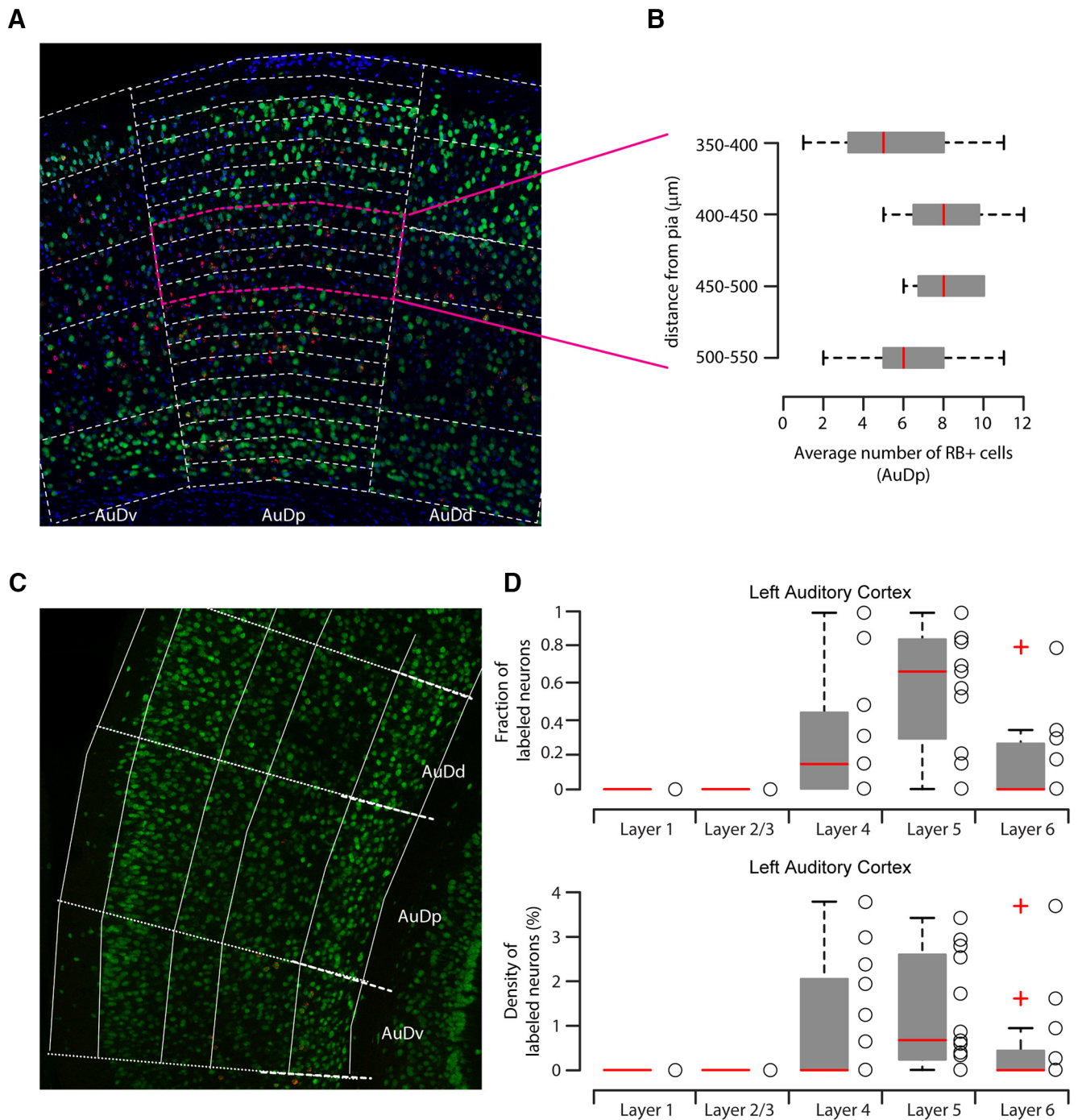


Figure 3. The 50 μm step analysis of L4 retrograde-labeled neurons in the right AC and quantification of L4 corticostriatal neurons in the left AC. **A**, Representative image of NeuN (green), DAPI (blue), and red RB (red) staining of dorsal (AuDd), primary (AuDp), and ventral (AuDv) AC with superimposed 50 μm step grid from pia to white matter (white lines). **B**, Detailed quantification of NeuN⁺/red RB⁺ double-positive neurons in the right primary AC, showing that the distribution of double-positive neurons was continuous for the whole thickness of L4 and not localized on the boundary with L2/L3 and L5. **C**, Representative image of NeuN (green), DAPI (blue), and red RB (red) staining of dorsal (AuDd), primary (AuDp) and ventral (AuDv) AC. The grid with normalized distance from pia is superimposed in white and was used to determine the layer distribution of NeuN⁺ and/or red RB⁺ neurons. L1 boundaries were adjusted based on DAPI staining (dashed white line). **D**, Quantification of fraction or density of double-labeled neurons in left AC. Box plots represent median value and distribution.

AAV-Chr2-tdTomato, titer 4×10^{12} GC/ml (rAAV9-CAG-hChR2-tdtomato, UNC Gene Therapy Center Vector Core);

AAV-flex-Chr2-YFP, titer 1.4×10^{13} GC/ml (pAAV-EF1a-doublefloxed-hChR2(H134R)-EYFP-WPRE-HGHpA, Addgene viral prep #20298-AAV1).

Stereotaxic injections: basic surgical procedures. As described in our previous studies (Rock et al., 2016, 2017; Zurita et al., 2018a,b; Bertero et al., 2019, 2020), mice were initially anesthetized with isoflurane (3%; 1 L/min O₂ flow) and head-fixed on a stereotaxic frame (Model 1900; Kopf

Instruments) using nonrupture ear bars. Anesthesia was maintained at 1%–1.5% isoflurane for the duration of the surgery. A warming pad was used to maintain body temperature during the procedure. Standard aseptic technique was followed for all surgical procedures. Injections were performed using a pressure injector (Nanoinject II; Drummond Scientific) mounted on the stereotaxic frame. Injections were delivered through a borosilicate glass injection pipette (Wiretrol II; Drummond Scientific) with a taper length of ~ 30 mm and a tip diameter of ~ 50 μm . The pipette remained in place for 5 min before starting

Table 2. Quantification of fraction or density of double-labeled neurons in left AC

Fraction	L1	L2/3	L4	L5	L6
	0	0	0	0.200	0.800
	0	0	0	0.667	0.333
	0	0	1.000	0	0
	0	0	0.300	0.700	0
	0	0	0.000	1.000	0
	0	0	0.143	0.571	0
	0	0	0.857	0.143	0
	0	0	0	1.000	0
	0	0	0.476	0.524	0
	0	0	0.143	0.857	0
	0	0	0	0.833	0.167
Minimum	0	0	0	0	0
25% Percentile	0	0	0	0.200	0
Median	0	0	0.143	0.667	0
75% Percentile	0	0	0.476	0.857	0.286
Maximum	0	0	1.000	1.000	0.800
Density	L1	L2/3	L4	L5	L6
	0%	0%	0%	0.59%	3.70%
	0%	0%	1.94%	3.43%	0%
	0%	0%	1.24%	2.94%	1.61%
	0%	0%	0%	0%	0%
	0%	0%	0.64%	2.54%	0%
	0%	0%	0%	0.66%	0.94%
	0%	0%	0%	0%	0%
	0%	0%	2.38%	0.33%	0%
	0%	0%	2.99%	0%	0%
	0%	0%	0%	0.86%	0%
	0%	0%	0%	0.39%	0%
	0%	0%	3.79%	2.80%	0%
	0%	0%	0%	1.72%	0.26%
Minimum	0%	0%	0%	0%	0%
25% Percentile	0%	0%	0%	0.17%	0%
Median	0%	0%	0%	0.66%	0%
75% Percentile	0%	0%	2.16%	2.67%	0.60%
Maximum	0%	0%	3.79%	3.43%	3.70%

injecting at 1 nl/s rate, 15 s waiting period after each nanoliter, and was left in place for 5 min after the injection to avoid viral backflow along the injection tract. Both male and female mice, between P35–P40 at the time of the injection, were used in these experiments.

Coordinates for injections are as follows: right AC (2.6 mm posterior and 4.5 mm lateral from bregma, 0.9 mm below the surface of the brain), right striatum (1.4 mm posterior and 3.35 mm lateral from bregma, 2.8 mm below the surface of the brain), right MGB (2.8 mm posterior and 2 mm lateral from bregma, 2.8 mm below the surface of the brain). Red retrobeads (RBs, Lumafluor) or 4% Fluorogold (Fluorochrome) was injected at a rate of 7 nl/min in the right striatum (30 nl and 20 nl injected volume, respectively). In contrast, viral preparations were injected at a rate of 4 nl/min in the right MGB (30 nl injected volume) or in the right AC (50 nl injected volume).

Quantification of red RB-positive (RB⁺) neurons in the AC. After washing in PBS, the slices were mounted on microscope slides, and images were taken with an Olympus SZX7 microscope. Five images of 100- μ m-thick slices of AC were selected, rotated, cropped, and the brightness/contrast was adjusted in ImageJ to identify the AC according to the Allen Brain Atlas. Dorsal, primary, and ventral areas of the AC were identified using the overlaid reference images. Representative slices were selected based on their anteroposterior localization according to the Allen Brain Atlas references in millimeters from bregma: -3.38 , -3.28 , -3.08 , -2.98 , -2.78 (see Fig. 2B).

Image postprocessing was performed with Adobe Photoshop by overlaying the epifluorescence images onto confocal images taken with a Carl Zeiss LSM-710 confocal microscope. Tile scan images of 3- μ m-thick single stacks were acquired at 20 \times magnification and 8-bit depth with ZEN software (Carl Zeiss). The two images were aligned using

anatomic landmarks, such as the rhinal fissure and the white matter. The distance from the pia to the white matter was normalized to 1000 μ m. AC layer boundaries were determined, as previously described (Ji et al., 2016; Bertero et al., 2020), as normalized depth from pia: layer 1 (L1) = 0–160 μ m; L2/L3 = 161–374 μ m, L4 = 375–520 μ m, L5 = 521–790 μ m; layer 6 (L6) = 791–1000 μ m. A grid according to these values was overlaid onto the images. L1 and L2/L3 boundaries were adjusted according to the NeuN density and Allen Mouse Brain reference Atlas when needed.

Neurons double-labeled for DAPI and NeuN, and the triple-labeled for red RBs, DAPI, and NeuN were manually counted with Cell Counter plug-in from ImageJ in each layer. The same approach was applied for the quantification of double-labeled neurons in the contralateral AC. The distribution of double-labeled neurons spanning the L4 was further confirmed in randomly sampled slices by superimposing a 50 μ m step grid from pia to white matter. For these experiments, ACp double-positive neurons were manually counted in 350–400, 400–450, 450–500 and 500–550 μ m steps from pia. Statistical differences of the CS neurons distributions within AC layers were analyzed by one-way ANOVA.

In vitro slice preparation and recordings. We allowed 2–4 weeks for viral expression, 4 d for red RB injections only. Mice were anesthetized with isoflurane and decapitated. Coronal slices (300 μ m) containing the area of interest (AC or auditory striatum) were sectioned on a vibratome (VT1200S; Leica Microsystems) in a chilled cutting solution containing the following (in mM): 100 choline chloride, 25 NaHCO₃, 25 D-glucose, 11.6 sodium ascorbate, 7 MgSO₄, 3.1 sodium pyruvate, 2.5 KCl, 1.25 NaH₂PO₄, 0.5 CaCl₂. These slices were incubated in oxygenated ACSF in a submerged chamber at 35°C–37°C for 30 min and then at room temperature (21°C–25°C) until recordings were performed. ACSF contained the following (in mM): 126 NaCl, 26 NaHCO₃, 10 D-glucose, 2.5 KCl, 2 CaCl₂, 1.25 NaH₂PO₄, 1 MgCl₂; osmolarity was \sim 290 Osm/L.

Whole-cell recordings were performed in 31°C–33°C ACSF. Thin-walled borosilicate glass pipettes (Warner Instruments) were pulled on a vertical pipette puller (PC-10; Narishige) and typically were in the range of 3–5 M Ω resistance when filled with a cesium-based intracellular solution, which contained the following (in mM): 110 CsOH, 100 D-gluconic acid, 10 CsCl₂, 10 HEPES, 10 phosphocreatine, 1 EGTA, 1 ATP, and 0.3%–0.5% biocytin. IPSCs were recorded in the voltage-clamp configuration with a holding potential of 0 mV (the calculated reversal potential for glutamatergic excitatory conductances). Intrinsic properties were recorded in the current-clamp configuration using a potassium-based intracellular solution at 31°C–33°C. Potassium-based intracellular solution contained the following (in mM): 120 potassium gluconate, 20 KCl, 10 HEPES, 10 phosphocreatine, 4 ATP, 0.3 GTP, 0.2 EGTA, and 0.3%–0.5% biocytin). Intrinsic properties of CS-L4 pyramidal neurons were performed on red RB⁺ neurons 370–530 μ m deep from pia. Signals were sampled at 10 kHz and filtered at 4 kHz. Pharmacological blockers used were as follows: CPP (5 μ M; Tocris Bioscience), NBQX (10 μ M; Abcam), and gabazine (12.5 μ M; Abcam). Hardware control and data acquisition were performed by Ephus (www.ephus.org) (Suter et al., 2010).

The resting membrane potential (V_m) was calculated in current-clamp mode ($I=0$) immediately after breaking in. Series (R_s) and input resistance (R_{in}) were calculated in voltage-clamp mode ($V_{hold} = -70$ mV) by giving a -5 mV step, which resulted in transient current responses. R_s was determined by dividing the voltage step amplitude by the peak of the capacitive current generated by the voltage step. The difference between baseline and steady-state hyperpolarized current (ΔI) was used to calculate R_{in} using the following formula: $R_{in} = -5 \text{ mV}/\Delta I - R_s$. Subthreshold and suprathreshold membrane responses in the current-clamp mode were elicited by injecting -100 to 500 pA in 50 pA increments at V_{rest} . The first resulting action potential (AP) at rheobase (I threshold, the minimal current of infinite duration, experimentally limited to 1 s, required to generate an AP) was analyzed for AP half-width. The spike frequency adaptation (SFA) ratio was measured at the current step that gave the closest APs firing rate to 20 Hz and calculated dividing the third instantaneous frequency by the fifth.

Chr2 photostimulation. Thalamic neurons transfected with AAV-ChR2-tdTomato showed red fluorescent-positive axons in the AC. To minimize Chr2 expression and transfection efficiency variability, we

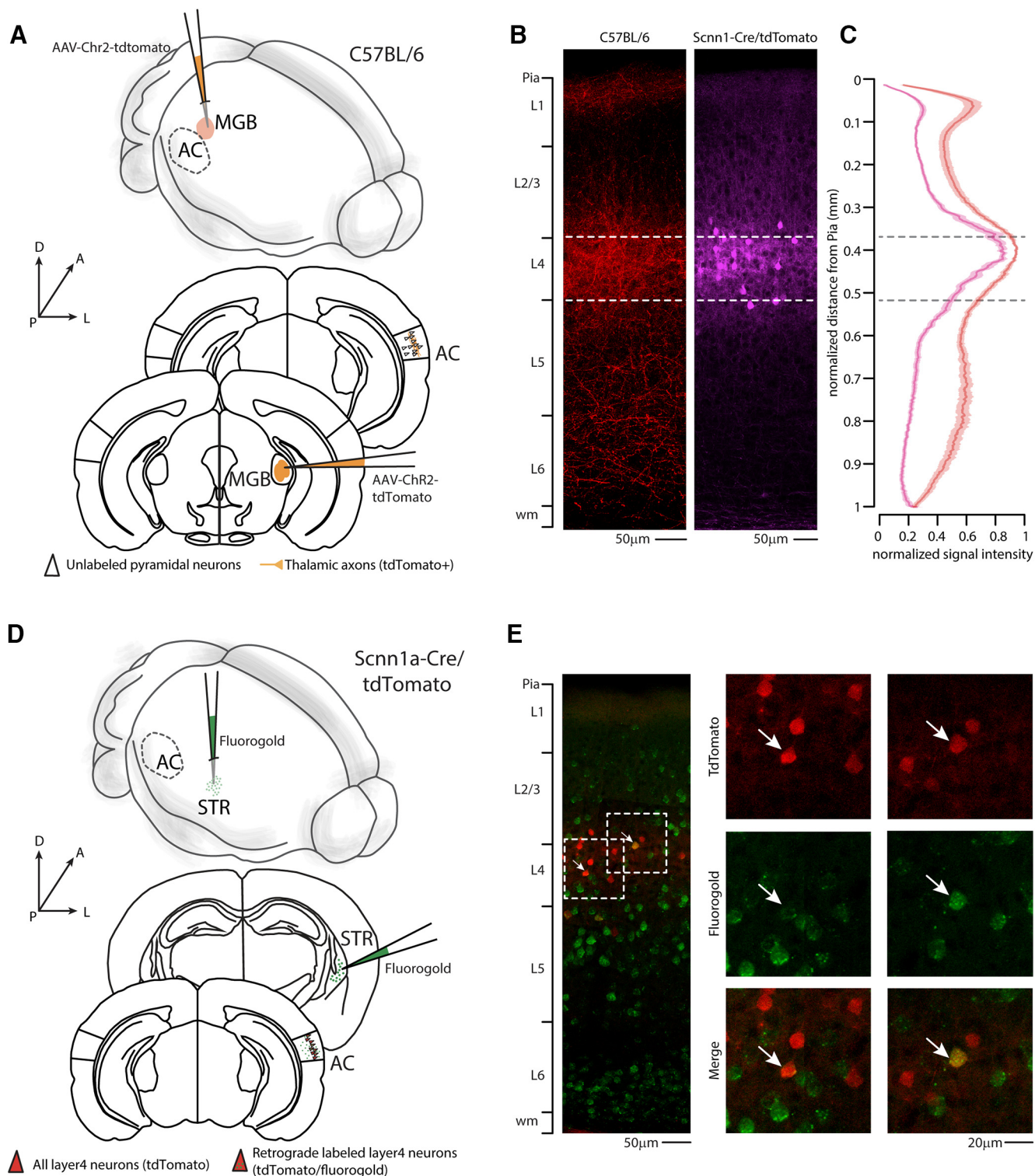


Figure 4. Identification/characterization of L4 and Fluorogold retrograde labeling of L4 corticostriatal neurons in Scnn1-tdTomato transgenic mouse line. **A**, Top, Schematic of the injection site in 3D. Bottom, Schematic of the Allen Brain Atlas tables and coordinates used for injections and imaging; 30 nl of AAV-Chr2-tdTomato was injected in the right MGB, while imaging was performed on the ipsilateral AC of C57BL/6 mice. **B**, Left, Representative high-resolution confocal image of C57BL/6 primary AC expressing tdTomato in the thalamic axons of the right AC. Scale bar, 50 µm. Right, Representative high-resolution confocal image of Scnn1-tdTomato primary AC preferentially expressed in L4 neurons. Scale bar, 50 µm. **C**, Quantification of laminar distribution of the normalized tdTomato signal intensity of the thalamic axons (red line) and L4 neurons (purple line) ($N = 12$ slices from 3 animals from 2 litters). Data are mean \pm SEM. **D**, Top, Schematic of the injection site in 3D. Bottom, Schematic of the Allen Brain Atlas tables and coordinates used for injections and imaging; 20 nl of 4% Fluorogold solution was injected in the right striatum, while imaging was performed on the ipsilateral AC of double-heterozygous Scnn1a-Cre/tdTomato mice. **E**, Two representative high-resolution confocal images of L4 primary AC. Red represents tdTomato preferentially expressed in L4 neurons. Green represents Fluorogold. Arrows indicate double-positive CS-L4 neurons. Scale bar, 20 µm.

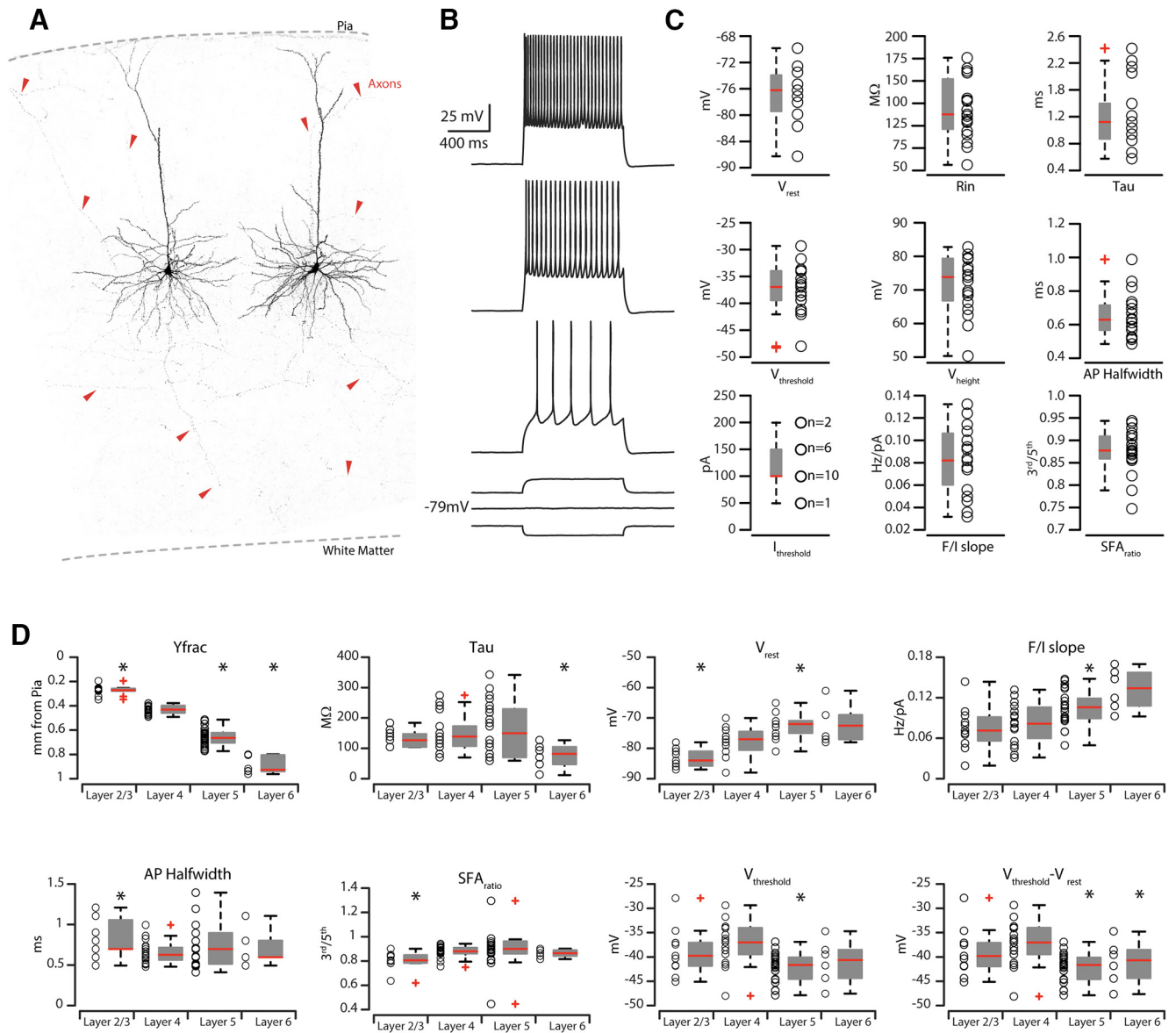


Figure 5. Electrophysiological properties of CS-L4 neurons compared with other corticostriatal neurons in different layers. **A**, High-resolution confocal images of two biocytin-filled CS-L4 neurons. Red arrowheads point at labeled axons from the two patched cells spanning all layers and going toward the white matter. **B**, Train of APs recorded in retrograde-labeled CS-L4 neurons during step of current injections (1.0 s, from -50 to 200 pA pulses with increments of 50 pA each step). **C**, Summary plot of the following: V_{rest} , resting membrane potential; R_{in} , input resistance; τ , membrane time constant; V_{thres} , AP threshold voltage; V_{height} , AP height; $AP_{half-width}$, AP half-width; I_{thres} , AP current threshold; F/I_{slope} , SFA_{ratio} , AP SFA from CS-L4 neurons ($n = 18$), including group averages (\pm SEM). **D**, Summary plot of the comparison of intrinsic properties of corticostriatal pyramidal neurons across cortical layers. Graphs represent the following: Y_{frac} , average distance from pia (0); τ , membrane time constant; V_{rest} , resting membrane potential; F/I slope; $AP_{half-width}$, AP half-width; SFA_{ratio} , SFA between third and fifth AP; V_{thres} , AP threshold voltage; $V_{thres} - V_{rest}$, difference between the AP threshold voltage and resting membrane potential from $n = 11$ CS-L2/3 neurons, $n = 18$ CS-L4 neurons, $n = 15$ CS-L5 neurons, and $n = 6$ CS-L6 neurons, including group averages (\pm SEM).

Table 3. Intrinsic properties of L4 corticostriatal neurons

	Mean	SEM
Y_{frac} (mm)	0.43	0.01
R_{in} (MOhm)	123.68	9.92
τ (ms)	1.28	0.13
V_{rest} (mV)	-77.58	0.94
$V_{threshold}$ (mV)	-37.34	0.99
V_{height} (mV)	71.76	1.94
AP half-width (ms)	0.65	0.03
I_{thres} (pA)	123.68	8.86
F/I slope (Hz/pA)	0.08	0.01
SFA ratio (third/fifth)	0.88	0.01

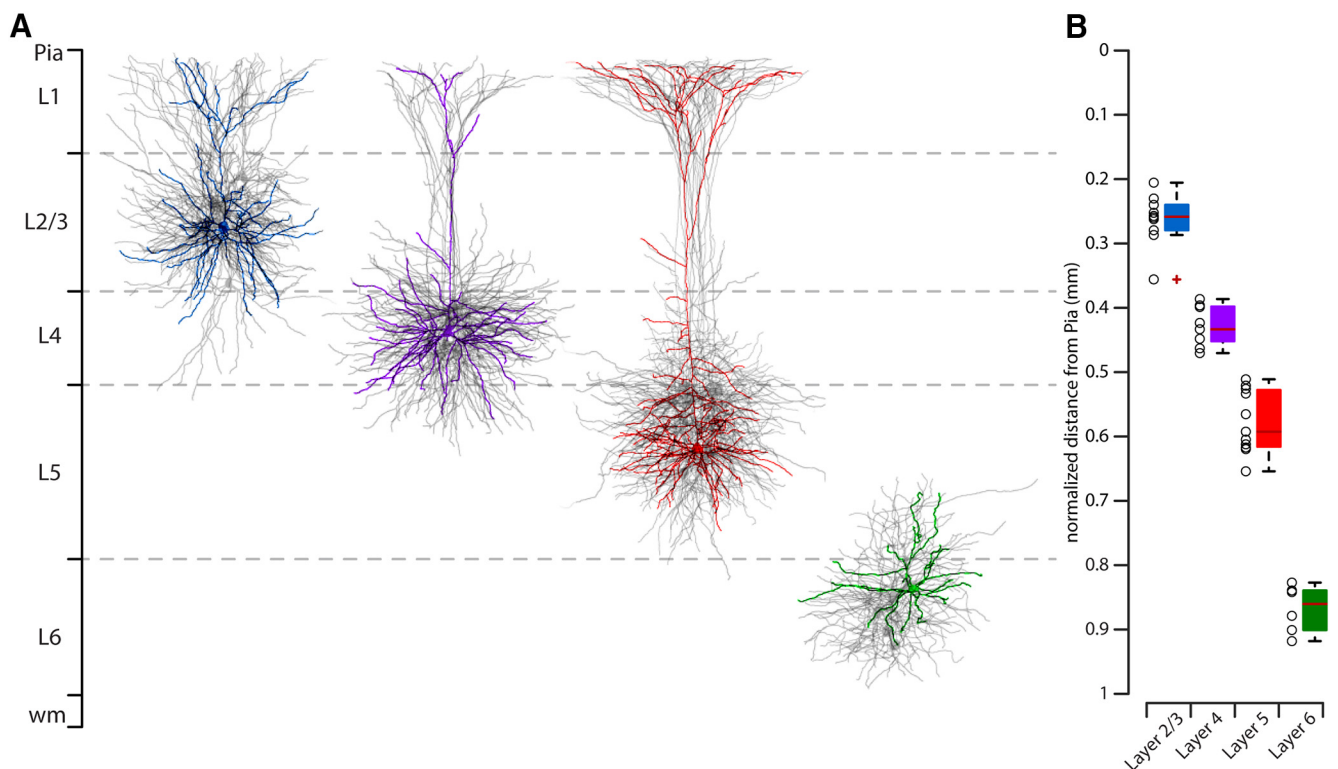
recorded from animals whose injection in the MGB was clean (no leak in other structures) and centered on the target. EPSC, IPSC, and current-clamp experiments (see figures) were performed on red bead⁺ cells, and GFP (G42⁺) neurons at a cortical depth of 380 – 520 μ m from pia, coupled with photostimulation with 488 nm wavelength blue LED (CoolLED pE excitation system) and a $60\times$ water-immersion objective. Unless differently stated in Results, the power used for photostimulation was as follows: $0.1, 4.7, 7, 9.7$ mW/mm².

Parv neurons in the AC were transfected with a local injection of AAV-flex-Chr2-YFP combined with red RBs injected in the right striatum. Whole-cell patch-clamp recordings on red RB⁺ CS-L4 neurons were achieved in voltage-clamp configuration holding the cells at 10 mV, coupled with 488 nm wavelength blue LED and $60\times$ water-immersion objective at a power of 0.1 – 1 mW/mm². $N = 7$ neurons from 2 animals from the same litter.

Table 4. Intrinsic properties of corticostriatal neurons

	L2/L3		L4		L5		L6		<i>p</i>		
	Mean	SEM	Mean	SEM	Mean	SEM	Mean	SEM	L2/3 vs L4	L4 vs L5	L4 vs L6
Y_{frac} (mm)	0.27	0.01	0.43	0.01	0.66	0.02	0.9	0.03	<0.0001*	<0.0001	0.0001
R_{in} (M Ω)	114	10.61	123.68	9.92	147.86	17.83	166.83	18.25	0.6506	0.0742	0.0612
τ (ms)	1.13	0.07	1.28	0.13	1.4	0.17	0.65	0.15	0.6899	0.9326	0.0433
V_{rest} (mV)	-83.09	0.87	-77.58	0.94	-72.77	0.71	-71.67	2.68	0.0037	0.0002*	0.0706
$V_{threshold}$ (mV)	-38.86	1.47	-37.34	0.99	-42.14	0.61	-41.11	1.86	0.3138	0.0002	0.2028
$V_{threshold} - V_{rest}$ (mV)	44.23	1.7	40.24	1.33	30.63	0.86	30.56	2.74	0.3193	<0.0001*	0.0327
AP half-width (ms)	0.83	0.07	0.65	0.03	0.73	0.05	0.7	0.09	0.0112	0.4719*	0.8735*
$I_{threshold}$ (pA)	131.82	15.48	123.68	8.86	113.64	11.48	108.33	20.07	0.9233*	0.4145*	0.3222*
Fast afterhyperpolarization (ms)	-13.61	1.47	-17.27	0.81	-9.84	1.41	-5.94	2.62	0.0683	0.0006	0.0118
F/I slope (Hz/pA)	0.08	0.01	0.08	0.01	0.11	0.01	0.13	0.01	0.4434*	0.0033*	0.1715
SFA ratio (third/fifth)	0.8	0.02	0.88	0.01	1.05	0.11	0.86	0.01	0.0019*	0.2447*	0.3239
SFA ratio (overall)	0.9	0.04	0.93	0.01	0.97	0.01	0.99	0.02	0.4911*	0.0012*	0.0068*

*Rank-sum test.

**Figure 6.** Layer distribution of corticostriatal neurons. **A**, Morphologic reconstruction of all L2/L3 (blue), L4 (purple), L5 (red), and L6 (green) biocytin-filled neurons. **B**, Normalized soma distance from pia for all four group of 3D reconstructed neurons.

Chr2/halo photostimulation. Thalamic neurons transfected with AAV-Chr2-tdTomato showed RFP-positive axons in the AC, whereas Parv neurons transfected with AAV-flex-Halo-YFP showed local somata and axons in the AC. To minimize variability of Chr2 and Halo expression and transfection efficiency, we recorded from animals whose injection in the MGB was clean (no leak in other structures) and centered on the target, and in which Halo⁺ neurons were present in the whole cortical thickness and at a higher intensity (center of the injection site). 488 nm blue LED (CoolLED pE excitation system) intensity was set to elicit at least 20 mV CS-L4 RB⁺ neuron membrane depolarization, while 567 nm amber LED (CoolLED pE excitation system) intensity and duration were set on the minimal power to silence L4 Halo⁺ neuron activity nearby. E/I experiments were performed at a holding current of -60, -20, and 0 mV (IV curve showed linearity, data not shown) with 488 nm and 567 nm intensity set on nearby L4 Halo⁺ neurons.

ChetaTC terminal photostimulation. CS-L4 neurons transfected with AAV-flex-ChetaTC-YFP showed YFP-positive axons in the auditory

striatum. To minimize ChetaTC expression and transfection efficiency variability, we recorded in the same striatal slice, with the highest density of transfected axons across different animals ($N = 20$ neurons, from 4 mice from 2 litters). We recorded IPSCs and EPSCs from randomly chosen cells in the striatum during photoactivation of CS-L4 axon terminals with 480 nm wavelength blue LED (CoolLED pE excitation system) and 60 \times water-immersion objective at a power of 7 mW/mm².

Histology. During whole-cell recordings, neurons were filled with an internal solution containing 0.3%–0.5% biocytin. Filled neurons were held for at least 20 min, and then the slices were fixed in a formalin solution (neutral buffered, 10% solution; Sigma-Aldrich) for 1–5 d at 4°C. The slices were washed well in PBS (6 times, 10 min per wash) and placed in a 4% streptavidin (AlexaFluor-488, -594, or -680 conjugated; Invitrogen) solution (498 μ l 0.3% Triton X-100 in PBS, 2 μ l streptavidin per slice). Slices were allowed to incubate in this solution at 4°C overnight, then washed well in PBS (6 times, 10 min per wash) and mounted with Fluoromount-G (Southern Biotechnology) on a glass microscope

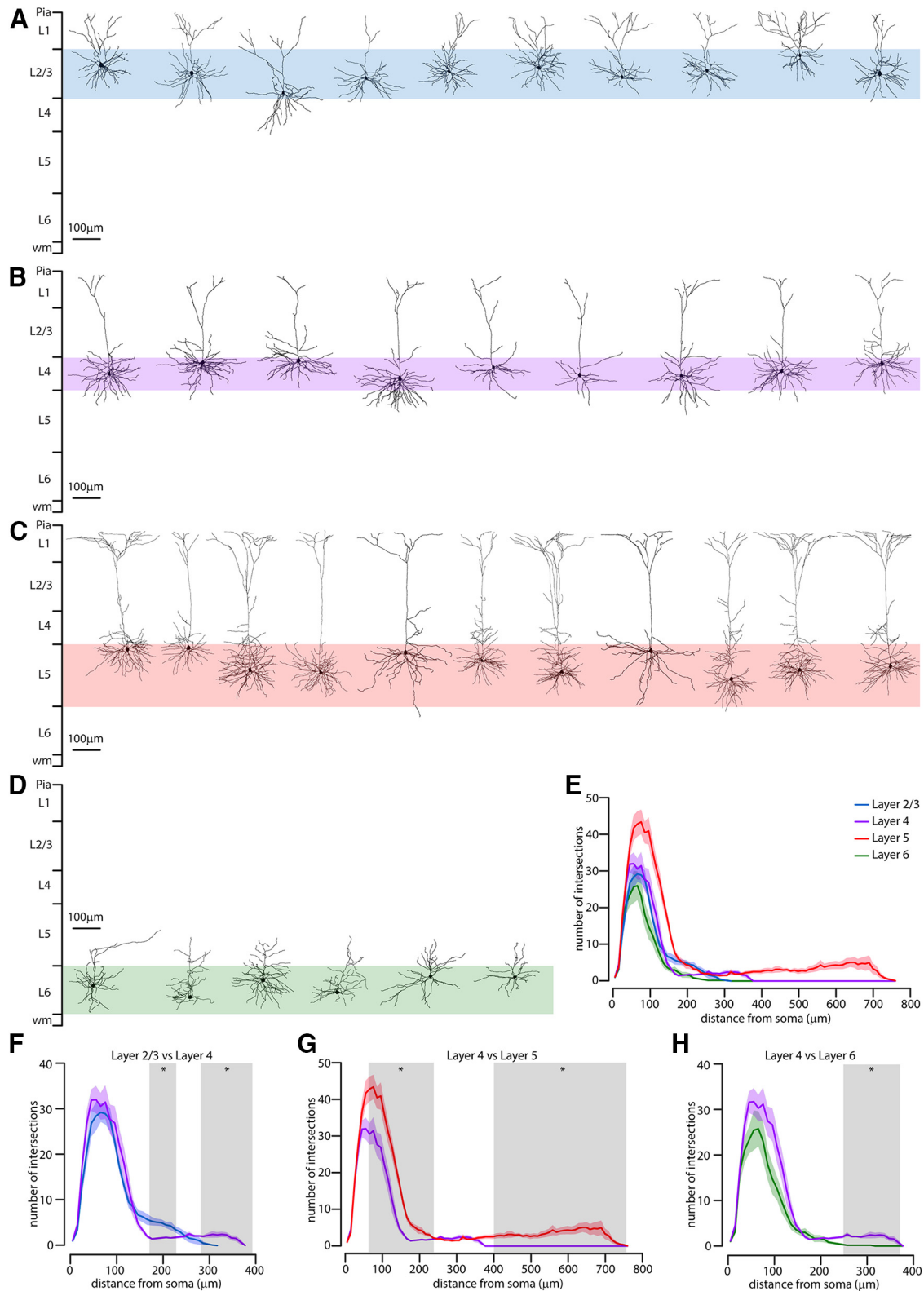


Figure 7. Anatomical characterization of corticostriatal pyramidal neurons. **A**, Morphologic reconstruction of the dendrites of L2/L3 corticostriatal neurons ($n = 10$ from 5 animals). **B**, Morphologic reconstruction of the dendrites of L4 corticostriatal neurons ($n = 9$ from 8 animals). **C**, Morphologic reconstruction of the dendrites of L5 corticostriatal neurons ($n = 11$ from 6 animals). **D**, Morphologic reconstruction of the dendrites of L6 corticostriatal neurons ($n = 6$ from 5 animals). **E**, Overall Sholl profile (\pm SEM) of the four analyzed neuronal groups, color-coded for layers, expressed as number of intersection of dendrites and shells of $10\ \mu\text{m}$ radius increments from soma. **F**, Comparison of the Sholl profile (\pm SEM) of L2/L3 corticostriatal neurons (blue) compared with CS-L4 neurons (purple). Gray area represents the distance from soma where the two populations have statistically significant difference in the number of intersections (rank-sum test, $p < 0.05$). **G**, Comparison of the Sholl profile (\pm SEM) of CS-L4 neurons (purple) compared with L5 corticostriatal neurons (red). Gray area represents the distance from soma where the two populations have statistically significant difference in the number of intersections (rank-sum test, $p < 0.05$). **H**, Comparison of the Sholl profile (\pm SEM) of CS-L4 neurons (purple) compared with L6 corticostriatal neurons (green). Gray area represents the distance from soma where the two populations have statistically significant difference in the number of intersections (rank-sum test, $p < 0.05$).

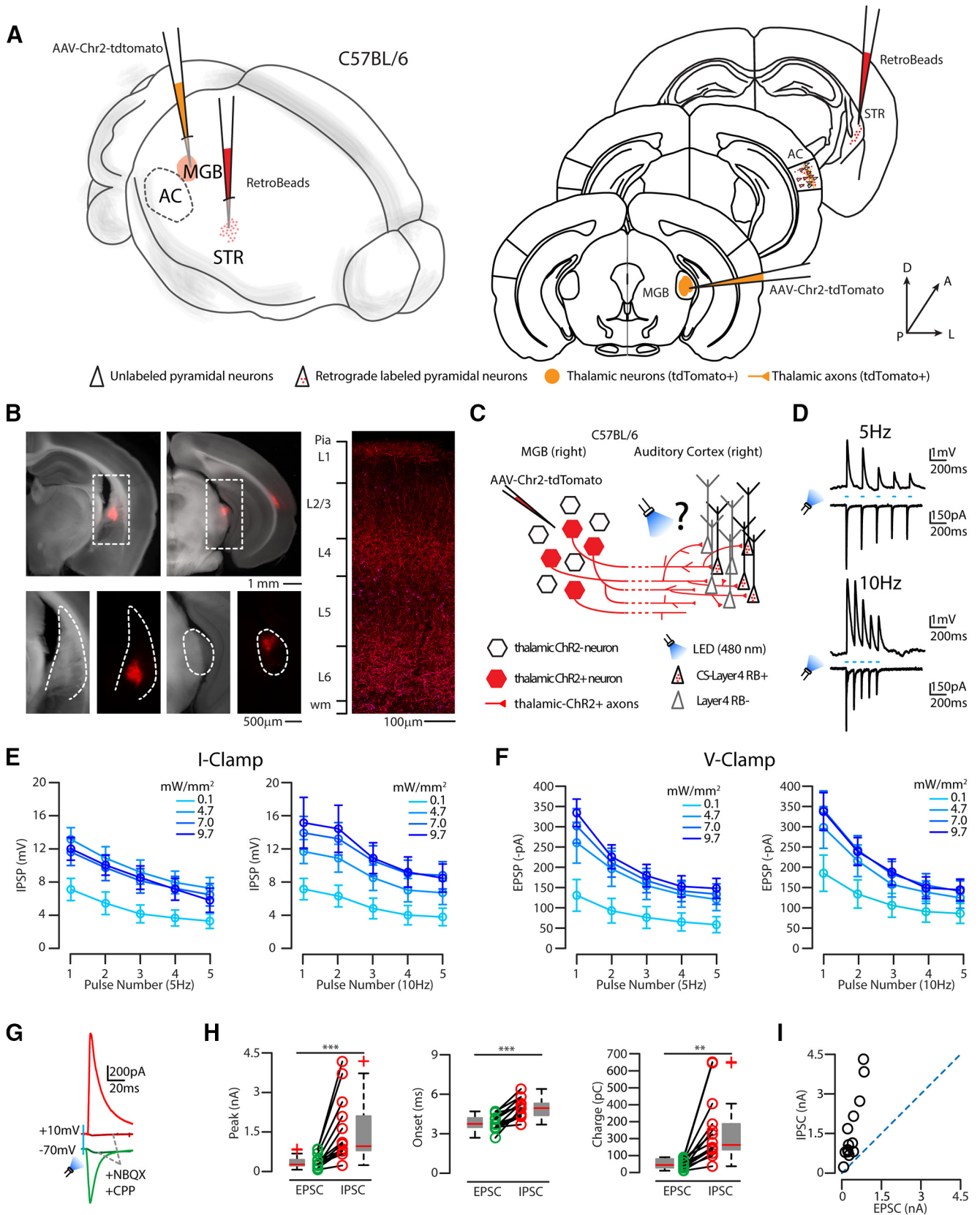


Figure 8. Thalamic monosynaptic excitatory and feedforward disinaptic inputs onto CS-L4 neurons. **A**, Left, Schematic of the injection sites in 3D. Right, Schematic of the Allen Brain Atlas tables and coordinates used for injections and imaging; 30 nl of red RBs was injected in the right striatum, 30 nl of AAV-Chr2-tdTomato was injected in the right MGB, while imaging and recordings were performed in the ipsilateral AC of C57BL/6 mice. **B**, Top left, Bright field and red fluorescence overlay of low-magnification images of the injection site in the striatum. Scale bar, 1 mm. Top right, Bright field and red fluorescence overlay of low-magnification picture of the injection site in the MGB. Scale bar, 1 mm. Bottom left, Bright field and red fluorescence picture of higher magnification of dotted square in the top left (striatum, anatomic boundaries indicated by the dotted line). Scale bar, 500 µm. Bottom right, Bright field and red fluorescence picture of higher magnification of dotted square in the top right (dotted line indicates MGB, anatomic boundaries). Scale bar, 500 µm. Right, Representative high-resolution confocal image of

Table 5. Thalamic inputs on CS-L4 pyramidal neurons

Pulse 1		Pulse 2		Pulse 3		Pulse 4		Pulse 5	
Mean	SEM	Mean	SEM	Mean	SEM	Mean	SEM	Mean	SEM
IC 5Hz (mV)									
7.08	1.34	5.41	1.36	4.12	1.08	3.63	0.97	3.25	0.88
11.61	1.63	9.71	1.56	8.13	1.49	7.22	1.44	6.44	1.36
13.14	1.42	10.87	1.38	9.17	1.47	7.93	1.37	7.24	1.29
12.00	1.38	10.02	1.22	8.52	1.42	7.11	1.32	5.77	1.46
IC 10 Hz (mV)									
7.09	1.29	6.24	1.31	4.75	1.25	3.93	1.18	3.71	1.06
11.65	1.45	10.84	1.69	8.47	1.54	6.96	1.42	6.65	1.43
13.91	2.00	13.20	1.96	10.52	1.83	8.97	1.63	8.77	1.65
15.14	3.08	14.41	2.86	10.85	1.87	9.15	1.84	8.43	1.70
VC 5 Hz (pA)									
-130.93	39.07	-93.05	30.34	-76.38	26.87	-65.38	22.20	-58.63	19.68
-260.91	50.44	-196.62	43.46	-154.97	34.42	-133.21	31.45	-121.19	27.92
-302.47	42.41	-211.68	35.75	-167.40	29.90	-141.71	26.23	-134.03	25.40
-334.64	33.82	-226.16	29.28	-179.61	27.68	-153.02	26.15	-148.14	24.68
VC 10 Hz (pA)									
-185.30	44.76	-133.90	34.86	-105.99	29.50	-90.40	25.90	-85.95	24.51
-298.14	51.44	-216.06	39.18	-157.55	30.95	-138.54	27.95	-124.59	25.67
-341.44	46.71	-242.21	35.64	-182.96	31.26	-155.67	28.49	-140.83	25.55
-337.63	46.52	-238.68	34.36	-188.17	31.90	-149.17	26.95	-144.22	26.47

slide. Confocal images were taken with a Carl Zeiss LSM-710 microscope at 40 \times magnifications. Image adjustment was performed in ImageJ (National Institutes of Health) for brightness/contrast corrections and pseudo coloring. Neurons were morphologically reconstructed in three dimensions using the Simple Neurite Tracer plug-in on ImageJ software (Schindelin et al., 2012).

Immunohistochemistry. Mice were transcardially perfused with 4% PFA, brains were dissected, postfixed overnight at 4 $^{\circ}$ C, and coronal sections (100 μ m tick) were obtained with a vibratome (Leica Microsystems). Immunohistochemical procedures were performed on free-floating sections using the following: rabbit anti-RFP (for tdTomato, 1:500, Abcam, catalog #ab62341), chicken anti-GFP (for YFP and GFP, 1:1000, Abcam, catalog #ab13970), rabbit anti-Parv (1:500, Abcam, catalog #ab11427), rabbit anti-NeuN (1:1000, Cell Signaling, catalog #24307S) primary antibodies, followed by AlexaFluor-633 goat anti-rabbit IgG (1:500, Invitrogen), AlexaFluor-594 goat anti-rabbit IgG (1:500, Invitrogen), and AlexaFluor-488 goat anti-chicken IgG (1:500, AbCam) secondary antibodies. Briefly, 100- or 300- μ m-thick slices were incubated 1 h at room temperature with blocking solution (PBS with 0.3% Triton X-100 and 5% goat serum), and overnight at 4 $^{\circ}$ C with primary antibody solution (blocking solution with the appropriate combination of primary antibodies) with gentle shaking. After 16–24 h, slices were thoroughly washed with PBS containing 0.3% Triton

X-100 at least 3 times for at least 10 min each wash, and then incubated 2 h at room temperature with secondary antibody solution (blocking solution with the appropriate combination of secondary antibodies). Before mounting, the slices were rewashed at least 3 times in PBS containing 0.3% Triton X-100 for at least 10 min each wash and then mounted in Fluoromount-G with or without DAPI (Southern Biotechnology). Confocal images were taken with a Carl Zeiss LSM-710 microscope at 10 \times -20 \times -40 \times magnifications with an appropriate filter set for DAPI, AlexaFluor-488/-594/-633. Image adjustment was performed with ImageJ (National Institutes of Health) or Adobe Photoshop for brightness/contrast corrections and pseudo coloring.

Data and statistical analysis. Error bars in all the figures represent SEM. Data analysis was performed offline using custom MATLAB (The MathWorks) routines. Group data represent the mean \pm SEM. Group comparisons were made using the rank-sum test for non-normal data distributions and *t* test for normally distributed data (assessed with Lilliefors's test), with significance defined as *p* < 0.05. In a subset of data, group comparisons were made using one-way ANOVA, with significance defined as *p* < 0.05 and *p* < 0.01.

Results

To determine the corticofugal contribution of different layers of the AC on striatal innervation, we used a retrograde approach, injecting red RBs in the right auditory striatum. After 2–5 d, we quantified the retrogradely labeled neurons in each layer of the right AC (Fig. 1). As expected, the highest fraction of bead-labeled neurons was in L5 and L2/L3 (Znamenskiy and Zador, 2013; Ponvert and Jaramillo, 2019), but we found a significant fraction also in L4 (fraction of labeled neurons: L2/3 = 0.28 \pm 0.02; L4 = 0.27 \pm 0.02; L5 = 0.36 \pm 0.02; L6 = 0.09 \pm 0.01; for detailed quantification, see Fig. 2 and Table 1), spanning the whole layer (Fig. 3A,B). Surprisingly, expressing this quantification as the density of labeled neurons per layer, we found that L4 and L5 have the same percentage of cells projecting to the striatum (density of labeled neurons: L2/3 = 12.5 \pm 1.5%; L4 = 21.0 \pm 1.5%; L5 = 21.8 \pm 2.02%; L6 = 5.3 \pm 0.7%) (for detailed quantification, see Fig. 2). The distribution of double-labeled neurons spanning the L4 was further confirmed in randomly sampled slices by superimposing a 50 μ m step grid from pia to white matter. Detailed quantification of NeuN/red RBs double-

←

tdTomato (red) expressing thalamic axons and red RB⁺ neurons (magenta) in the ipsilateral AC layer reference on the left bar. Scale bar, 100 μ m. **C**, Schematic represents the experimental paradigm: thalamic neurons expressing Chr2 projects to L4 of the ipsilateral AC, in which CS-L4 neurons (identified by red bead labeling) were recorded while flashing a blue LED (480 nm). **D**, Top two, Representative I-clamp (top) and V-clamp (bottom) trace while flashing the blue light at 5 Hz for 5 pulses. Bottom two, Representative I-clamp (top) and V-clamp (bottom) trace while flashing the blue light at 10 Hz for 5 pulses. **E**, Summary plot of I-clamp recordings of EPSPs, while flashing the blue light at 5 or 10 Hz for 5 pulses, at four different light powers. Data are mean \pm SEM. **F**, Summary plot of V-clamp recordings of EPSCs, while flashing the blue light at 5 or 10 Hz for 5 pulses, at four different light powers. Data are mean \pm SEM. **G**, Representative trace of EPSCs (green trace) and IPSCs (red trace) recorded from a CS-L4 neuron. Dark green (EPSCs) and dark red traces (IPSCs) were recorded after bath application of NBQX and CPP and demonstrate that thalamic inputs are excitatory only and that inhibition is disynaptic on Chr2 photoactivation. **H**, Quantification of EPSC and IPSC parameters: peak (pA), onset of response (ms), and charge (pC). Box plots represent median value and distribution. **p* < 0.05. ***p* < 0.01. ****p* < 0.005. **I**, Summary plot represents each cell E/I value, with all neurons patched distributed in the top left quadrant of the distribution indicating an E/I ratio < 1.

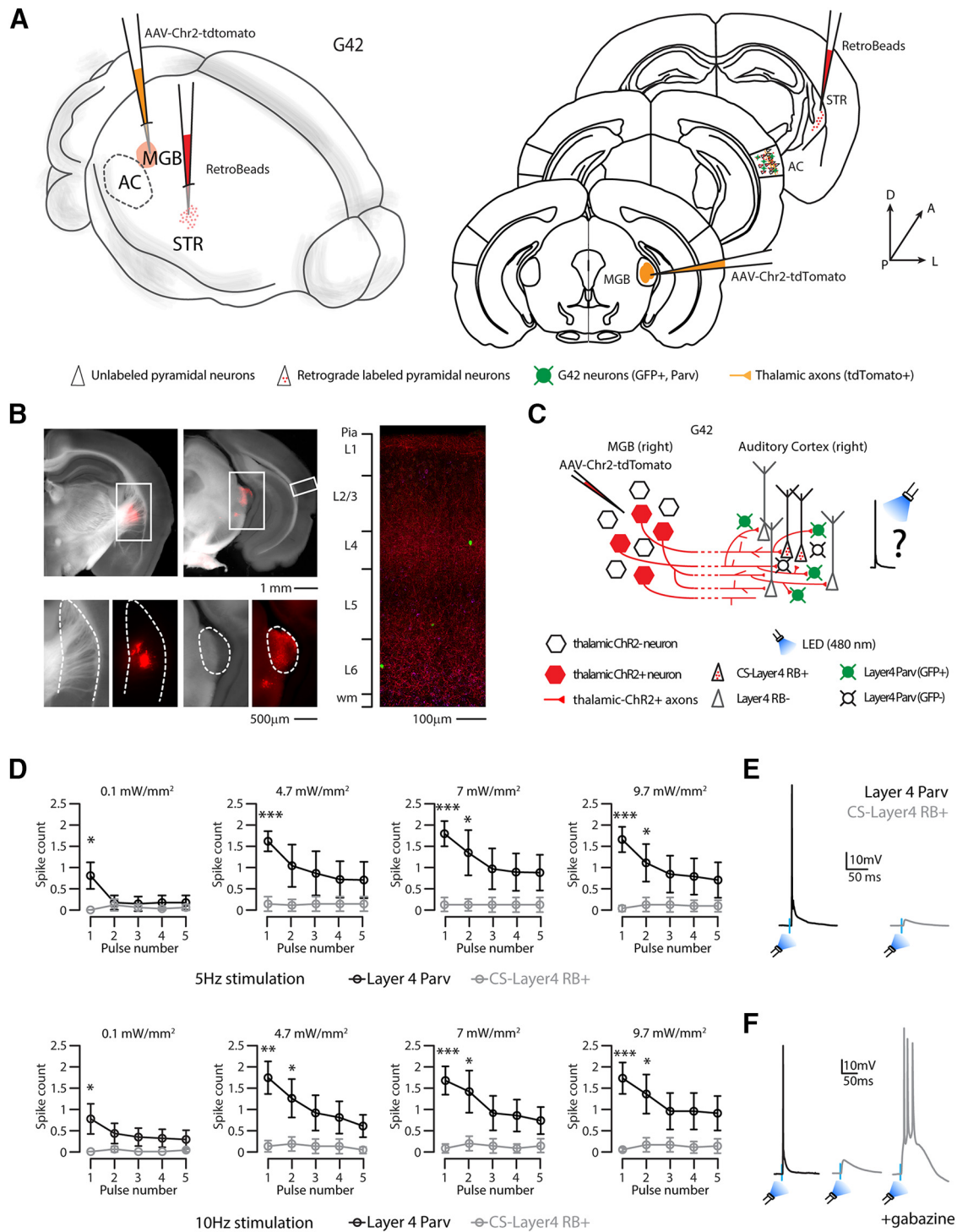


Figure 9. Photostimulation of thalamic projections evoked AP in Parv, but not CS-L4 neurons. **A**, Left, Schematic of the injection sites in 3D. Right, Schematic of the Allen Brain Atlas tables and coordinates used for injections and imaging; 30 nl of red RBs was injected in the right striatum, 30 nl of AAV-Chr2-tdTomato was injected in the right MGB, while imaging and recordings were performed in the ipsilateral AC of G42 mice expressing GFP in a subset of Parv neurons in the brain. **B**, Top left, Bright field and red fluorescence overlay of low-magnification images of the injection site in the striatum. Scale bar, 1 mm. Top right, Bright field and red fluorescence overlay of low-magnification picture of the injection site in the MGB. Scale bar, 1 mm. Bottom left, Bright field and red fluorescence picture of higher magnification of dotted square in the top left (striatum, anatomic boundaries indicated by the dotted line). Scale bar, 500 µm. Bottom right, Bright field and red fluorescence picture of higher magnification of dotted square in the top right (the dotted line indicates MGB, anatomic boundaries). Scale bar, 500 µm. Right, Representative high-resolution confocal image of tdTomato (red) expressing thalamic axons, red RB⁺ neurons (magenta), and Parv-GFP⁺ neurons (green) in the ipsilateral AC layer reference on the left bar. Scale bar, 100 µm. **C**, Schematic represents the experimental paradigm: thalamic neurons expressing ChR2 projects to L4 of the ipsilateral AC, in which CS-L4 neurons (identified by red bead labeling) and L4 Parv neurons (GFP⁺) were recorded while flashing a blue LED (480 nm). **D**, Top, Quantification of average spike counts in Parv (black) and CS-L4 neurons (gray) while flashing the blue LED at 5 Hz for 5 pulses at 4 different powers. Parv neurons fire APs with significant higher probability at the first pulse of light compared with CS-L4 neurons, at all light powers used. Data are mean ± SEM. *N* = 7 pairs, 4 animals from 2 litters. **p* < 0.05. ***p* < 0.01. ****p* < 0.005. Bottom, Quantification of average spike counts in Parv (black) and CS-L4 neurons (gray) while flashing the blue LED at 10 Hz for 5 pulses at 4 different powers. Parv neurons fire APs with significant higher probability at the first (and second) pulse of light compared with CS-L4 neurons, at all light powers used. Data are mean ± SEM. *N* = 7 pairs, 4 animals from 2 litters. **p* < 0.05. ***p* < 0.01. ****p* < 0.005. **E**, Representative traces of an L4 Parv

positive neurons in the right primary AC indicates that their distribution was continuous for the whole thickness of L4 and not localized on the boundary with L2/L3 or L5 (350–400: 5.6 ± 1.66 neurons; 400–450: 8.2 ± 1.16 neurons; 450–500: 8.2 ± 0.8 neurons; 500–550: 6.4 ± 1.43 neurons). The contralateral AC displayed a negligible fraction of CS-L4 double-labeled neurons, indicating that the major source of corticofugal connections is the ipsilateral AC (Fig. 3C,D; Table 2). Since L4 is described as the major thalamo-recipient layer of the AC (Cruikshank et al., 2002; Rose and Metherate, 2005; Lee and Winer, 2008), we confirmed that the peak of thalamic innervation corresponds to the peak of fluorescent neurons in the AC of the L4 transgenic mouse line (Scnn1a-Cre/tdTomato). Specifically, we injected AAV-Chr2-tdTomato in the right MGB of WT mice (Fig. 4A), to be compared with the laminar distribution of the reporter-expressing L4 neurons in Scnn1a/tdTomato mice (Fig. 4B). With this set of experiments, we identified L4 to be at a normalized distance from pia between 375 and 520 μm (Fig. 4C), in agreement with previous studies (Zhou et al., 2014; Ji et al., 2016). We also checked whether we could use the Scnn1a-Cre line to study the role of L4-CS projections onto striatal neurons. To this aim, we checked for labeled neurons in L4, which confirmed the retrograde labeling of L4 tdTomato-expressing neurons in this Cre-driver transgenic mouse line (Fig. 4D,E).

To better characterize this newly identified long-range corticostriatal (from now on: CS-L4) neural population in the AC, we performed whole-cell patch-clamp recordings of intrinsic properties and morphologic characterization of bead-labeled neurons in L4 of mice injected with red RBs in the ipsilateral auditory striatum. We patched only RB⁺ neurons in the range of 380–490 μm from pia (stricter than previously described) (Zhou et al., 2014; Ji et al., 2016), to exclude cells that laid too close to the boundaries with L2/L3 and L5, avoiding potential misclassification of CS-L4 neurons. We were able to recover the morphology of 9 of 19 patched CS-L4 neurons. High-resolution confocal images of biocytin-filled CS-L4 neurons showed that they exhibit a pyramidal morphology with a dense dendritic arborization in L4 and one or more branches reaching L1 (Fig. 5A). Interestingly, where the axons were fully visible, they showed arborizations in L2/L3 and L5, together with an axonal branch going toward the white matter (Fig. 5A). Basic electrophysiological properties of CS-L4 neurons ($n = 19$) included (Fig. 5B,C; Table 3) the following: resting membrane potential, -77.6 ± 0.9 mV; input resistance, 123 ± 9.9 M Ω ; membrane time constant, 1.3 ± 0.1 ms; rheobase, 123.7 ± 8.9 pA; AP threshold, -37.34 ± 0.99 mV; AP height, 71.76 ± 1.94 mV; AP half-width, 0.65 ± 0.03 ms; F/I slope, 0.08 ± 0.01 Hz/pA step; SFA (third/fifth) 0.88 ± 0.01 . All properties and their response to standard current steps were typical for pyramidal neurons (Winer, 1984; Mitani and Shimokouchi, 1985; Mitani et al., 1985; Metherate and Aramakis, 1999; Huggenberger et al., 2009).

In order to demonstrate that L4 corticostriatal neurons are different from corticostriatal neurons in other layers, we grouped the data on the basis of the soma location into four layer groups,

←

neuron (black trace) and a CS-L4 neuron (gray trace) recorded during blue LED photostimulation at minimal power to elicit an AP in the Parv neuron. A couple of GFP/red-bead⁺ neurons was considered a pair when their soma were closer than 100 μm . While all Parv neurons were firing an AP, none of the associated CS-L4 neurons could fire. $N = 10$ pairs, 4 animals from 1 litter. **F**, Representative traces of a L4 Parv neurons (black) and a CS-L4 neuron (gray) while flashing the light at the minimum power to elicit an AP in the Parv neuron. In the presence of gabazine, the same light power can elicit multiple APs in the CS-L4 neuron (right).

Table 6. Thalamic inputs on L4 G42 and CS-L4 neurons

	G42+ L4		CS-L4		<i>p</i>
	Mean	SEM	Mean	SEM	
5 Hz, 0.1 mW/mm ²					
Pulse 1	0.66	0.21	0.00	0.00	0.0210
Pulse 2	0.31	0.21	0.11	0.14	0.3147
Pulse 3	0.20	0.17	0.06	0.07	0.7308
Pulse 4	0.17	0.17	0.03	0.03	0.7308
Pulse 5	0.17	0.17	0.06	0.07	0.7308
5 Hz, 4.7 mW/mm ²					
Pulse 1	1.72	0.29	0.14	0.17	0.0017
Pulse 2	1.32	0.47	0.11	0.14	0.0210
Pulse 3	1.00	0.49	0.14	0.17	0.1189
Pulse 4	0.86	0.40	0.14	0.17	0.1678
Pulse 5	0.85	0.40	0.14	0.17	0.1678
5 Hz, 7 mW/mm ²					
Pulse 1	1.80	0.29	0.14	0.17	0.0017
Pulse 2	1.36	0.53	0.14	0.13	0.0536
Pulse 3	0.98	0.48	0.14	0.17	0.1189
Pulse 4	0.90	0.44	0.14	0.17	0.1678
Pulse 5	0.89	0.42	0.14	0.17	0.1189
5 Hz, 9.7 mW/mm ²					
Pulse 1	1.87	0.32	0.06	0.07	0.0006
Pulse 2	1.32	0.43	0.14	0.17	0.0210
Pulse 3	1.00	0.43	0.14	0.17	0.0699
Pulse 4	0.92	0.41	0.11	0.14	0.0699
Pulse 5	0.83	0.40	0.11	0.14	0.0699
10 Hz, 0.1 mW/mm ²					
Pulse 1	0.77	0.36	0.00	0.00	0.0699
Pulse 2	0.43	0.24	0.06	0.07	0.1923
Pulse 3	0.34	0.21	0.00	0.00	0.1923
Pulse 4	0.31	0.21	0.00	0.00	0.1923
Pulse 5	0.29	0.22	0.04	0.04	0.4615
10 Hz, 4.7 mW/mm ²					
Pulse 1	1.76	0.38	0.14	0.13	0.0006
Pulse 2	1.27	0.45	0.20	0.16	0.0816
Pulse 3	0.93	0.42	0.14	0.17	0.1189
Pulse 4	0.82	0.38	0.14	0.17	0.1678
Pulse 5	0.62	0.26	0.06	0.07	0.0699
10 Hz, 7 mW/mm ²					
Pulse 1	1.69	0.33	0.09	0.10	0.0006
Pulse 2	1.42	0.50	0.20	0.17	0.0495
Pulse 3	0.92	0.41	0.14	0.17	0.1189
Pulse 4	0.86	0.38	0.09	0.10	0.0699
Pulse 5	0.74	0.32	0.14	0.17	0.1189
10 Hz, 9.7 mW/mm ²					
Pulse 1	1.74	0.09	0.06	0.04	0.0006
Pulse 2	1.37	0.20	0.17	0.17	0.0495
Pulse 3	0.96	0.14	0.17	0.17	0.1678
Pulse 4	0.96	0.09	0.11	0.14	0.0699
Pulse 5	0.92	0.14	0.14	0.17	0.1189

corresponding to L2/L3, L4, L5, and L6 (see Materials and Methods), and compared their electrophysiological and anatomic properties. L4 corticostriatal neuron electrophysiological characterization indicates that these neurons were a separate class from those located in L2/L3, L4, L5, and L6 (Fig. 5D; Table 4). Particularly, L4 corticostriatal neurons were statistically different from L2/L3 corticostriatal neurons in V_{rest} ($L4 = -77.8 \pm 0.7$ mV; $L2/3 = -83.1 \pm 0.9$ mV, $p = 0.0037$, t test), AP half-width ($L4 = 0.65 \pm 0.03$ ms; $L2/3 = 0.83 \pm 0.07$ ms, $p = 0.0112$, t test), and SFA ($L4 = 0.88 \pm 0.01$ third/fifth; $L2/3 = 0.8 \pm 0.02$ third/fifth, $p = 0.0019$, rank-sum test; Fig. 5D; Table 4). On the other hand, L4 corticostriatal neurons differed from L5 corticostriatal neurons in V_{rest} ($L4 = -77.8 \pm 0.7$ mV; $L5 = -72.8 \pm 0.7$ mV, $p = 0.0002$, rank-sum test), V_{thresh} ($L4 = -37.3 \pm 1$ mV; $L5 =$

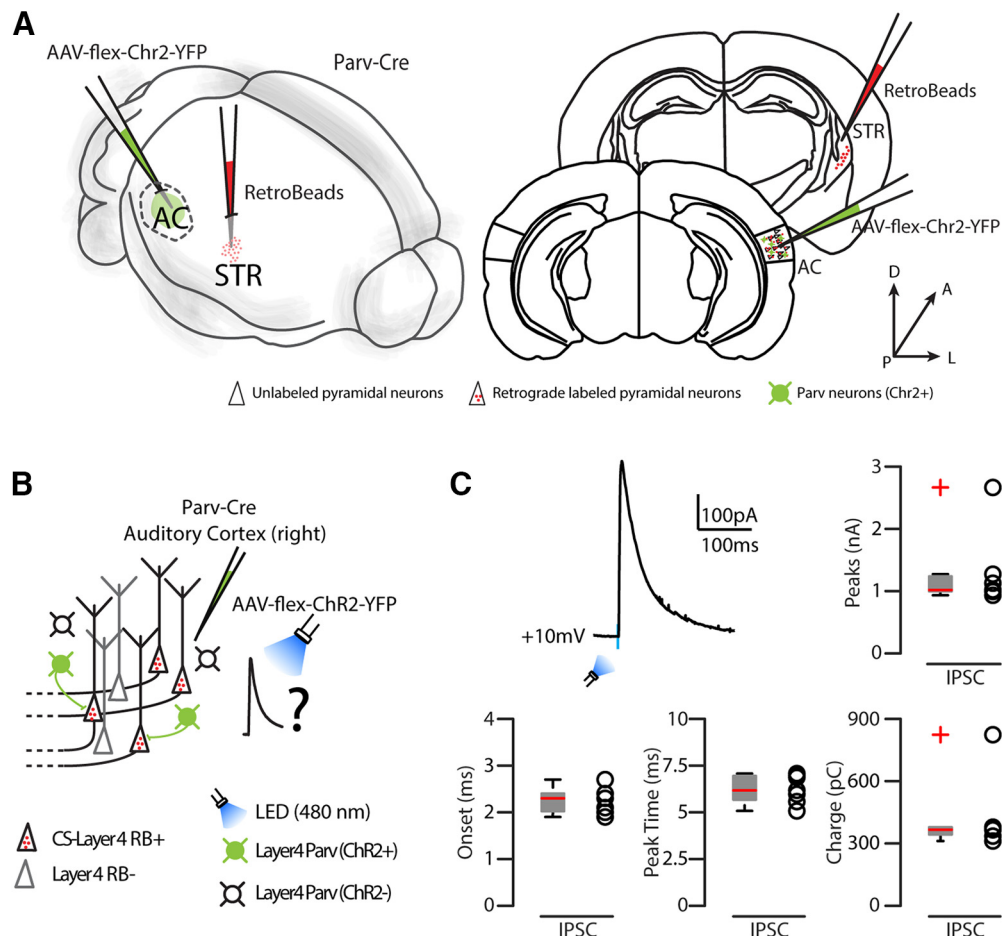


Figure 10. Parv-ChR2-evoked inhibitory inputs onto CS-L4 neurons. **A**, Left, Schematic of the injection sites in 3D. Right, Schematic of the Allen Brain Atlas tables and coordinates used for injections and imaging; 30 nl of red RBs was injected in the right striatum, 30 nl of AAV-flex-Chr2-YFP was injected in the right AC, while imaging and recordings were performed in the right AC of Parv-Cre transgenic mice. **B**, Experimental paradigm for photostimulation of Parv Chr2-positive GABAergic neurons while recording IPSCs from CS-L4 neurons identified by anatomic retrograde labeling. **C**, Example of IPSCs recorded at 10 mV from L4 CS neurons ($n=8$ neurons). Summary plot of IPSC peak (nA), onset (ms), peak time (ms), and charge (pC) recorded in CS-L4 neurons. Box plot and group averages (\pm SEM).

-42.14 ± 0.61 mV, $p=0.0002$, t test), $V_{\text{thresh}} - V_{\text{rest}}$ ($L4 = 40.2 \pm 1.3$ mV; $L5 = 30.6 \pm 0.9$ mV, $p < 0.0001$, rank-sum test), fast afterhyperpolarization ($L4 = -17.27 \pm 0.8$ ms, $L5 = -9.8 \pm 1.4$ ms, $p=0.0006$, t test), F/I slope ($L4 = 0.08 \pm 0.01$; $L5 = 0.11 \pm 0.01$ Hz/pA, $p=0.0033$, t test), and overall SFA ratio ($L4 = 0.93 \pm 0.01$; $L5 = 0.97 \pm 0.01$, $p=0.0012$, rank-sum test; Fig. 5D; Table 4). L4 corticostriatal neurons differed also from L6 corticostriatal neurons in tau ($L4 = 1.3 \pm 0.1$ ms; $L6 = 0.65 \pm 0.15$ pA, $p=0.0433$, t test), V_{rest} ($L4 = -77.8 \pm 0.7$ mV; $L6 = -71.7 \pm 2.7$ mV, $p=0.0706$, t test), $V_{\text{thresh}} - V_{\text{rest}}$ ($L4 = 40.2 \pm 1.3$ mV; $L6 = 30.56 \pm 2.7$ mV, $p=0.0327$, t test), fast afterhyperpolarization ($L4 = -17.27 \pm 0.8$ ms, $L6 = -5.94 \pm 2.62$ ms, $p=0.0118$, t test), and overall SFA ratio ($L4 = 0.93 \pm 0.01$; $L6 = 0.99 \pm 0.02$, $p=0.0068$, rank-sum test; Fig. 5D; Table 4). Therefore, these four populations of corticostriatal projecting neurons in L2/L3, L4, L5, and L6 of AC can be routinely differentiated by their distinct intrinsic electrophysiological properties.

Next, we tested the hypothesis that corticostriatal pyramidal neurons have different morphological properties according to their layer of origin (Figs. 6 and 7). We quantitatively analyzed the morphology of biocytin-filled L2/L3 ($n=10$), L4 ($n=9$), L5 ($n=11$), and L6 ($n=6$) corticostriatal pyramidal neurons. L5 corticostriatal pyramidal neurons had an extensive dendritic arborization in layer 1, a feature typical of thick-tufted pyramidal neurons in other cortical areas, whereas L2/L3, L4, and L6

corticostriatal pyramidal neurons lacked this feature (Figs. 6A and 7A–D). We empirically determined the location of biocytin-filled corticostriatal pyramidal neurons for each slice, measured as the normalized distance between the pia and the white matter. The soma locations of corticostriatal pyramidal neurons were significantly different from each other (L2/L3: 0.262 ± 0.013 mm, $n=10$; L4: 0.43 ± 0.1 mm, $n=9$; L5: 0.578 ± 0.015 mm, $n=11$; L6: 0.868 ± 0.015 mm, $n=6$; $p=0.00002$, $p=0.0002$, and $p=0.0004$, respectively, rank-sum test) (Fig. 6B). Next, we determined the main morphological features of the four populations of corticostriatal pyramidal neurons with a Sholl analysis of their 3D reconstructed dendritic arborization, confirming the morphologic differences between the L4 corticostriatal pyramidal neurons and those in other layers (Fig. 7E). Compared with L2/L3 corticostriatal neurons, CS-L4 pyramidal neurons were similar in the first 150 μ m from the soma, indicating that the basal dendrites have the same complexity in the two populations. Between 160 and 210 μ m from soma, they were less complex (since they have an apical dendrite reaching layer 1, while L2/L3 neurons lack this feature), while from 260 μ m from soma to the end of their apical dendrites, they were more complex (Fig. 7F). On the other hand, compared with L5 corticostriatal neurons, CS-L4 pyramidal neurons were less complex between 70 and 220 μ m from soma, indicating that L5 neurons have a denser basal dendrite organization, and at the very end of their apical

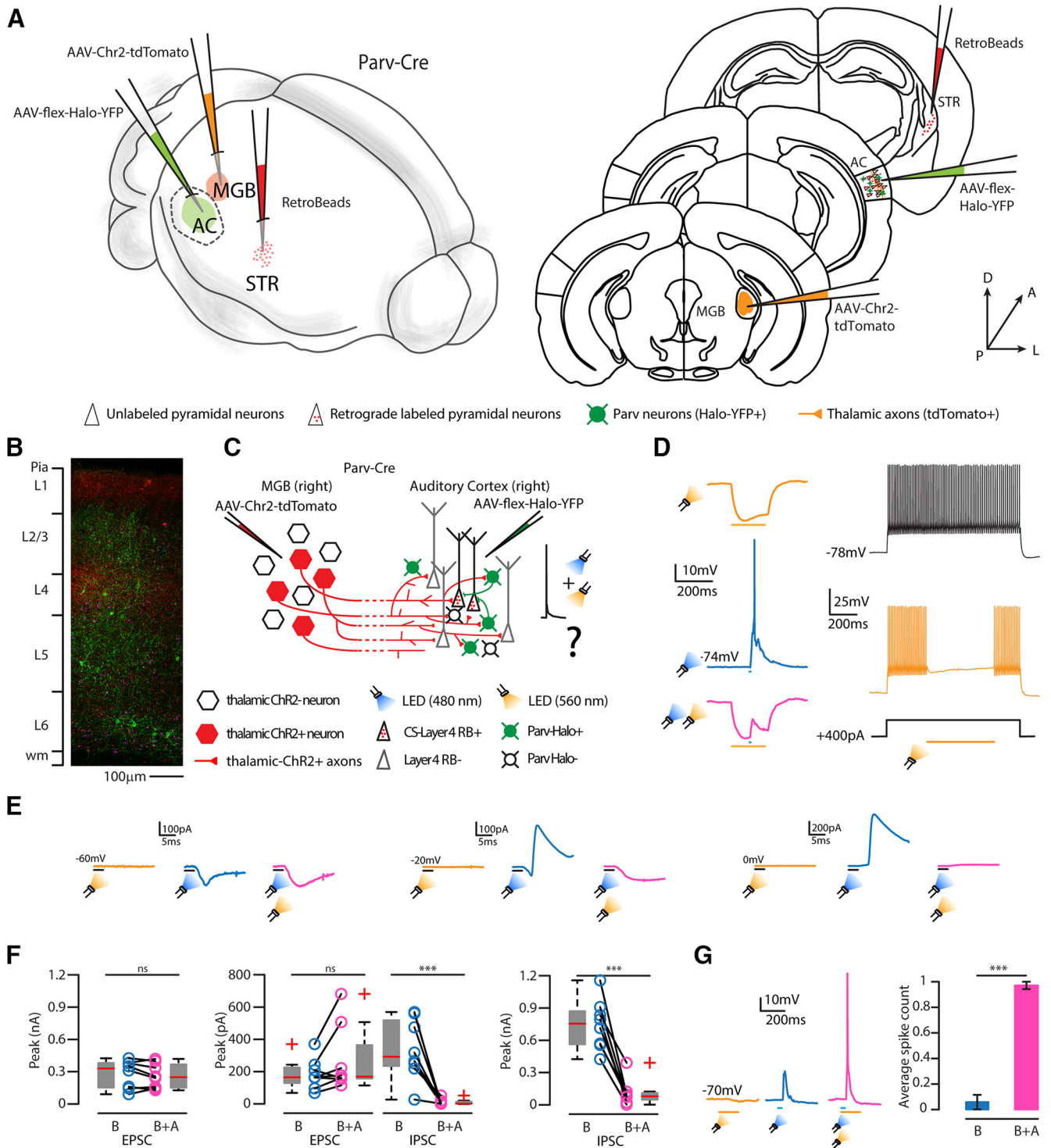


Figure 11. Suppression of CS-L4 neurons by Parv GABAergic neurons as a function of photoactivation of thalamic projections. **A**, Left, Schematic of the injection sites in 3D. Right, Schematic of the Allen Brain Atlas tables and coordinates used for injections and imaging; 30 nl of red RBs was injected in the right striatum, 30 nl of AAV-Chr2-tdTomato in the right MGB, and 100 nl of AAV-flex-Halo in the right auditory, where imaging and recordings were performed, of Parv-Cre transgenic mice. **B**, Representative high-resolution confocal image of tdTomato (red) expressing thalamic axons, red RB⁺ neurons (magenta), and YFP Halo⁺ Parv neurons (green) in the ipsilateral AC, with layer reference on the left bar. Scale bar, 100 µm. **C**, Schematic represents the experimental paradigm: thalamic neurons expressing Chr2 projects to L4 of the ipsilateral AC, in which CS-L4 neurons (identified by read-beads labeling) or L4 Parv neurons (Halo-YFP-positive) were recorded while flashing a blue LED (480 nm) alone or in combination with amber LED (560 nm). **D**, Representative recordings of a Parv neuron expressing Halo. Left traces, From top to bottom, Membrane hyperpolarization during a long pulse of amber light (orange); membrane depolarization and AP generation in response to a brief pulse of blue light (blue); the combination of both lights (pink) can prevent AP generation in response to thalamic inputs on the Parv neuron. Right traces, Fast-spiking AP train (black trace, top) of a Parv neuron expressing Halo during a 1 s current injection (black trace, bottom) without and with (orange trace, middle) amber light. APs were abolished entirely for the whole duration of amber light stimulation. **E**, Left, Representative traces of whole-cell recordings holding the membrane potential of CS-L4 neurons at -60 mV while flashing the amber light only (yellow trace, no effect), the blue light only (blue trace, light evoked EPSPs), or both amber and blue light (pink trace, no abolition of EPSPs). Middle, Representative traces of whole-cell recordings holding the membrane potential of CS-L4 neurons at -20 mV while flashing the amber light only (yellow trace, no effect), the blue light only (blue trace, light evoked EPSPs and IPSPs), or both amber and blue light (pink trace, no effect on EPSP, while IPSP is abolished). Right, Representative traces of whole-cell recordings holding the membrane potential of CS-L4 neurons at 0 mV while flashing the amber light only

dendrites (400 μm from soma and over) since they are shorter than L5 pyramidal neurons (Fig. 7G). Interestingly, the shared pyramidal morphology of these two populations, with one apical dendrite that reaches the upper cortical layers, is described by a similar number of intersections between 230 and 360 μm from the soma (Fig. 7G). Finally, the comparison between CS-L4 and L6 corticostriatal neurons revealed differences after 230 μm from the soma, as L6 neurons do not have elaborate apical dendrites (Fig. 7H).

These results demonstrate that the dendritic morphologies of CS-L4 neurons are different from those in other layers, which may be reflected in terms of specialized electrophysiological properties. Overall, these data demonstrate that CS-L4 neurons are a distinct population of corticostriatal pyramidal neurons.

Do CS-L4 neurons receive thalamic inputs?

Since cortical L4 has been described as the major thalamo-recipient layer of the AC (Rose and Metherate, 2005; Lee and Sherman, 2008; Schiff and Reyes, 2012; Vasquez-Lopez et al., 2017; Park and Geffen, 2020), we then characterized the direct thalamic inputs onto CS-L4 neurons. To this aim, we injected the right auditory thalamus (MGB) of C57BL/6 mice with AAV-Chr2-tdTomato in combination with red RBs in the right auditory striatum and performed whole-cell patch-clamp recordings of bead-labeled CS-L4 neurons in the AC (Fig. 8A–C). We activated Chr2⁺ thalamic axons with blue LED light (488 nm) for 3 ms at two different frequencies (5 and 10 Hz; see Fig. 8D). EPSCs were isolated by applying a command potential of -70 mV (the calculated reversal potential for GABAergic inhibitory conductance) at four increasing blue light power (0.1, 4.7, 7, 9.7 mW/mm²) through a 60 \times water immersion objective (Fig. 8D). The same light stimulation was applied to isolated EPSPs in I-clamp mode ($I=0$) (Fig. 8D). We found that CS-L4 neurons receive strong thalamic inputs, and increasing blue light power increased the EPSCs up to 3 times from minimal stimulation (number of CS-L4 neurons, $n=11$, Fig. 8E,F; for values, see Table 5), reaching up to -400 pA at the first flash of light, while both frequencies elicit depressing inputs. EPSP quantification (number of CS-L4 neurons, $n=12$) showed the same slope and behavior in I-clamp configuration, with values of up to 15.14 ± 3.08 mV at the first flash of light, Fig. 8E,F; for values, see Table 5). Despite the high excitatory inputs CS-L4 neurons receive, none of the patched neurons fired an AP on blue LED stimulation. We then asked whether this was because of excitation/inhibition unbalance, and we patched another set of CS-L4 neurons in C57BL/6 mice with the same injection paradigm. EPSCs and IPSCs were separated by applying a command potential of either -70 mV (the calculated reversal potential for

GABAergic inhibitory conductance) or 10 mV (the calculated reversal potential for glutamatergic excitatory conductance; Fig. 8G) while flashing blue light for 3 ms between 0.9 and 1 mW/mm². We found ($n=14$ neurons) high disynaptic inhibition (peak EPSCs: 378.36 ± 66.14 pA, peak IPSCs: 1522.47 ± 321.47 pA, $p=0.00176$, t test; charge EPSC: 50.66 ± 7.46 pC, charge IPSC: 246.79 ± 51.34 pC, $p=0.0008$, t test), as demonstrated by the suppression of both EPSCs and IPSCs applying excitatory synaptic blockers NBQX and CPP (Fig. 8G). This was also confirmed by onset analysis that showed that excitation was significantly faster (3.85 ± 0.15 ms) than inhibition (4.95 ± 0.2 ms, $p=0.00015$, t test), times compatible with monosynaptic and disynaptic mechanisms, respectively (Fig. 8H). As shown in Figure 8I, all patched cells showed an E/I ratio <1 (average: 0.28 ± 0.03).

How do thalamic inputs impact L4 parvalbumin neurons compared with CS-L4 pyramidal neurons?

We then asked which GABAergic neurons could supply such fast and local inhibition on thalamic stimulation, and we hypothesized that the main player could be local parvalbumin-expressing (Parv) neurons (Agmon and Connors, 1991; Gabernet et al., 2005; Verbny et al., 2006; Cruikshank et al., 2007). First, we assessed the direct thalamic inputs onto L4 Parv neurons compared with thalamic inputs onto CS-L4 pyramidal neurons by injecting the right auditory thalamus (MGB) of G42 (Chattopadhyaya et al., 2004) mice with AAV-Chr2-tdTomato in combination with red RBs in the right auditory striatum (Fig. 9A–C). We recorded 10 consecutive pairs of L4 G42 and CS-L4 neurons in the same column (i.e., the distance between soma <100 μm), holding them at the same membrane potential (-70 mV) while flashing the blue light for 1 ms at the minimum power to elicit an AP in the G42 neuron and used the same power on the neighboring beads-positive CS-L4 neuron. All pairs showed that the light power necessary to elicit an AP in G42 neurons generated an average EPSP of 4.87 ± 0.86 mV in CS-L4 neurons (Fig. 9E). We also performed multiple pulse stimulations at increasing light power (0.1, 4.7, 7, 9.7 mW/mm²) at two different frequencies (5 and 10 Hz) and quantified the number of APs of both cell types (Fig. 9D; number of consecutive pairs $n=7$; for values and statistics, see Table 6). Again, repeated light stimulation elicited depressing inputs, and G42 neuron spike probability decreased with the number of light stimuli in the train at all frequencies and all light powers. Overall, all pairs showed a significant difference in the first pulse of both frequencies, with G42 neurons firing one or more APs, while CS-L4 neurons failed to fire an AP at almost every trial, even at the highest light power used (Fig. 9D). These data were further supported by the fact that combining light stimulation with GABA(A) blockage (gabazine) also drove CS-L4 neurons to fire APs, indicating that a local source of inhibition was responsible for the lower spike probability of CS-L4 neurons on direct thalamic stimulation (Fig. 9F).

Do L4 parvalbumin neurons innervate CS-L4 pyramidal neurons?

To determine if L4 parvalbumin neurons were connected to CS-L4 neurons, we injected a cre-dependent AAV-flex-Chr2 in the right AC of Parv-Cre mice in combination with red RBs injected in the right striatum. We then recorded IPSCs in CS-L4 pyramidal neurons in the AC when flashing blue light through a 60 \times water immersion objective and showed that they receive strong inhibitory inputs from the surrounding Parv-Chr2⁺ neurons (Fig. 10). IPSCs characterization included the following: peak 1289.49 ± 233.20 mV, charge 423.16 ± 67.38 pC, peak time 6.27 ± 0.29 ms, onset 2.26 ± 0.10 ms ($n=7$ neurons from 2 animals from the same litter).

←

(yellow trace, no effect), the blue light only (blue trace, light evoked IPSP), or both amber and blue light (pink trace, IPSP is completely abolished). **F**, Left, Quantification of EPSC peak height holding the membrane potential of CS-L4 neurons at -60 mV while flashing the blue light only (B, blue) or both amber and blue light (B + A, pink). Middle, Quantification of EPSC and IPSC peak height holding the membrane potential of CS-L4 neurons at -20 mV while flashing the blue light only (B, blue) or both amber and blue light (B + A, pink). Right, Quantification of IPSC peak height holding the membrane potential of CS-L4 neurons at 0 mV while flashing the blue light only (B, blue) or both amber and blue light (B + A, pink). $N=8$ neurons, 3 animals from 2 litters. **G**, Left, Representative traces of I-clamp experiments on CS-L4 neurons while flashing the amber (yellow), blue (blue), or blue and amber together (pink). Bar plot of the quantification of the spike probability of CS-L4 neurons in response to blue light (B, blue) or blue and amber light (B + A, pink). Data are expressed as \pm SEM. Silencing local Parv-Halo⁺ neurons while stimulating the thalamic axon's excitatory inputs can drive CS-L4 neurons to fire APs. $N=7$ neurons, 3 animals from 2 litters. *** $p < 0.005$.

Do L4 parvalbumin neurons inhibit CS-L4 pyramidal neurons in response to thalamic inputs?

We directly manipulated the activity of local Parv neurons while stimulating thalamic axons in L4 of the AC to demonstrate that Parv neurons were responsible for the feedforward inhibitory circuit controlling CS-L4 APs in response to thalamic inputs. To this aim, we injected a cre-dependent inhibitory opsin (AAV-flex-Halo-YFP) in the right AC of Parv-Cre mice, in combination with AAV-Chr2-tdTomato in the right MGB and red RBs in the right auditory striatum (Fig. 11A–C). We first checked the efficacy of Halo expression in Parv neurons, performing light stimulation and current injections (Fig. 11D). We set the conditions in which a brief blue light pulse combined with sustained amber light was enough to suppress the AP evoked by blue light alone. Similarly, when injecting 1-s-long current steps and simultaneous flashing amber light was enough to suppress AP trains (Fig. 11D). Once demonstrated that we could control the activity of Parv-Halo⁺ neurons in the area of interest, we checked the E/I balance of CS-L4 neurons when local Parv neurons were silenced during thalamic stimulation. Amber light alone was not affecting CS-L4 neurons activity nor their excitatory inputs if combined with blue light (average EPSPs with blue light only: 279.59 ± 45.41 pA; average EPSP with blue and amber light: 259.58 ± 40.54 pA, $p = 0.7894$ rank-sum, number of neurons, $n = 8$) (Fig. 11E,F). However, while blue light alone was sufficient to elicit strong inhibitory inputs on CS-L4 neurons (average IPSPs with blue light only: 743.21 ± 82.04 pA, number of neurons, $n = 8$), the simultaneous silencing of Parv-Halo⁺ neurons significantly reduced IPSCs (average IPSPs with blue and amber light: 106.54 ± 42.67 pA, $p = 0.00016$, rank-sum, number of neurons, $n = 8$) up to 86% (Fig. 11F). This behavior was also observed when holding the neurons at -20 mV, where we could isolate both excitatory and inhibitory inputs: average EPSPs with blue light only = 183.93 ± 30.99 pA, average EPSP with blue and amber light = 271.45 ± 68.32 pA, $p = 0.2936$ (rank-sum, number of neurons, $n = 8$); average IPSPs with blue light only = 336.34 ± 61.93 pA, average IPSPs with amber and blue light = 10.20 ± 6.27 pA, $p = 0.00023$ (rank-sum, number of neurons, $n = 8$, equals 96% reduction). This demonstrated that local

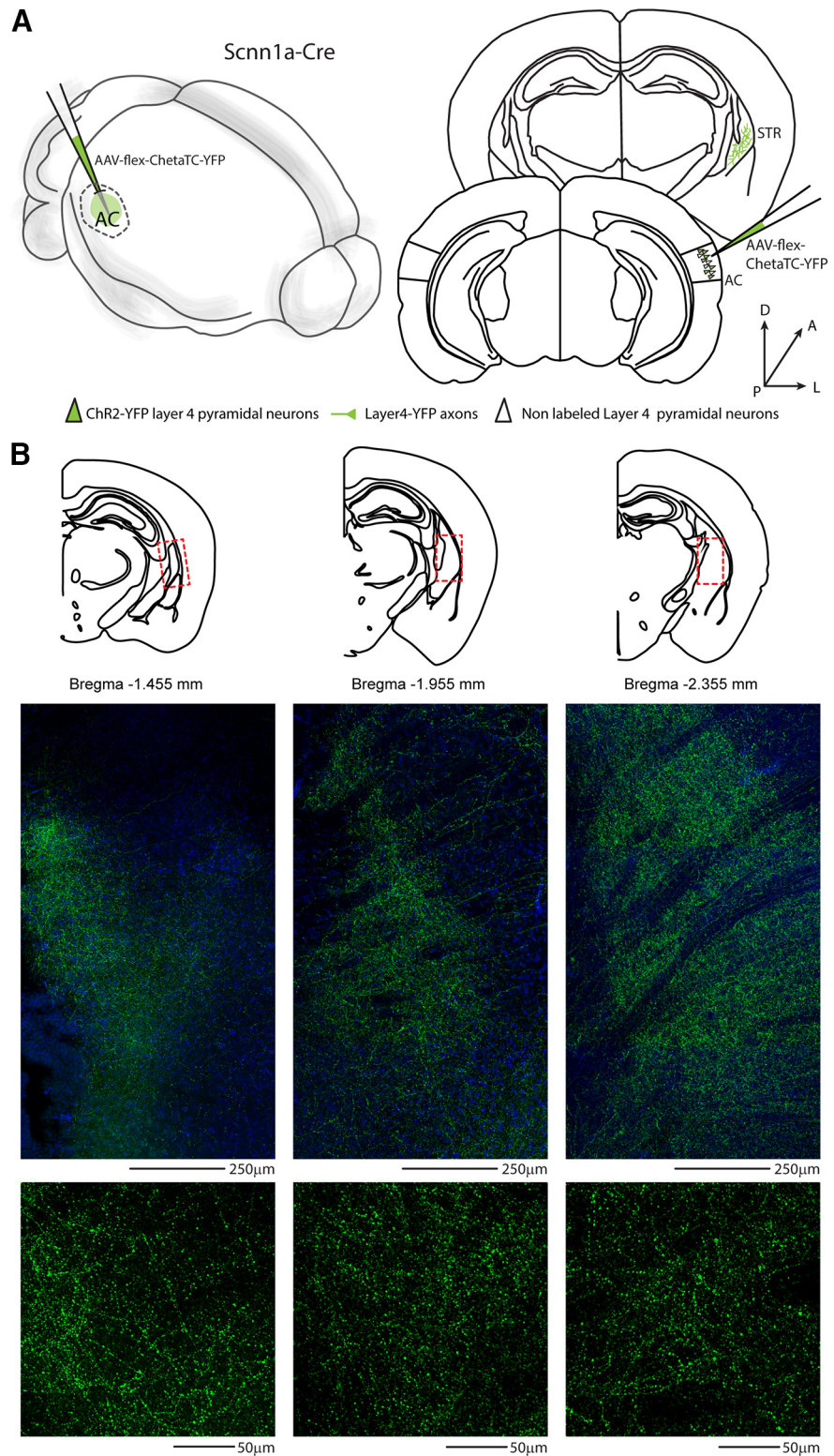


Figure 12. Distribution of L4 excitatory projections from the AC to the ipsilateral striatum. **A**, Left, Schematic of the injection sites in 3D. Right, Schematic of the Allen Brain Atlas tables and coordinates used for injections and imaging; 50 nl of AAV-flex-ChetaTC-YFP was injected in the right AC, while imaging was performed in the right auditory striatum of Scnn1a-Cre transgenic mice. **B**, Top, Allen Mouse Brain Atlas map of the location of the L4 excitatory projections from the AC to the dorsal auditory striatum. Red dashed line indicates the location of confocal images of middle panels. Middle, Confocal images of YFP-expressing fluorescent axons in the right striatum, with DAPI (blue) counterstain. Scale bar, 250 μ m. Bottom, 40 \times high-magnification confocal images from middle panels, showing the dense axonal arborization of CS-L4 pyramidal neurons in the dorsal auditory striatum. Scale bar, 50 μ m.

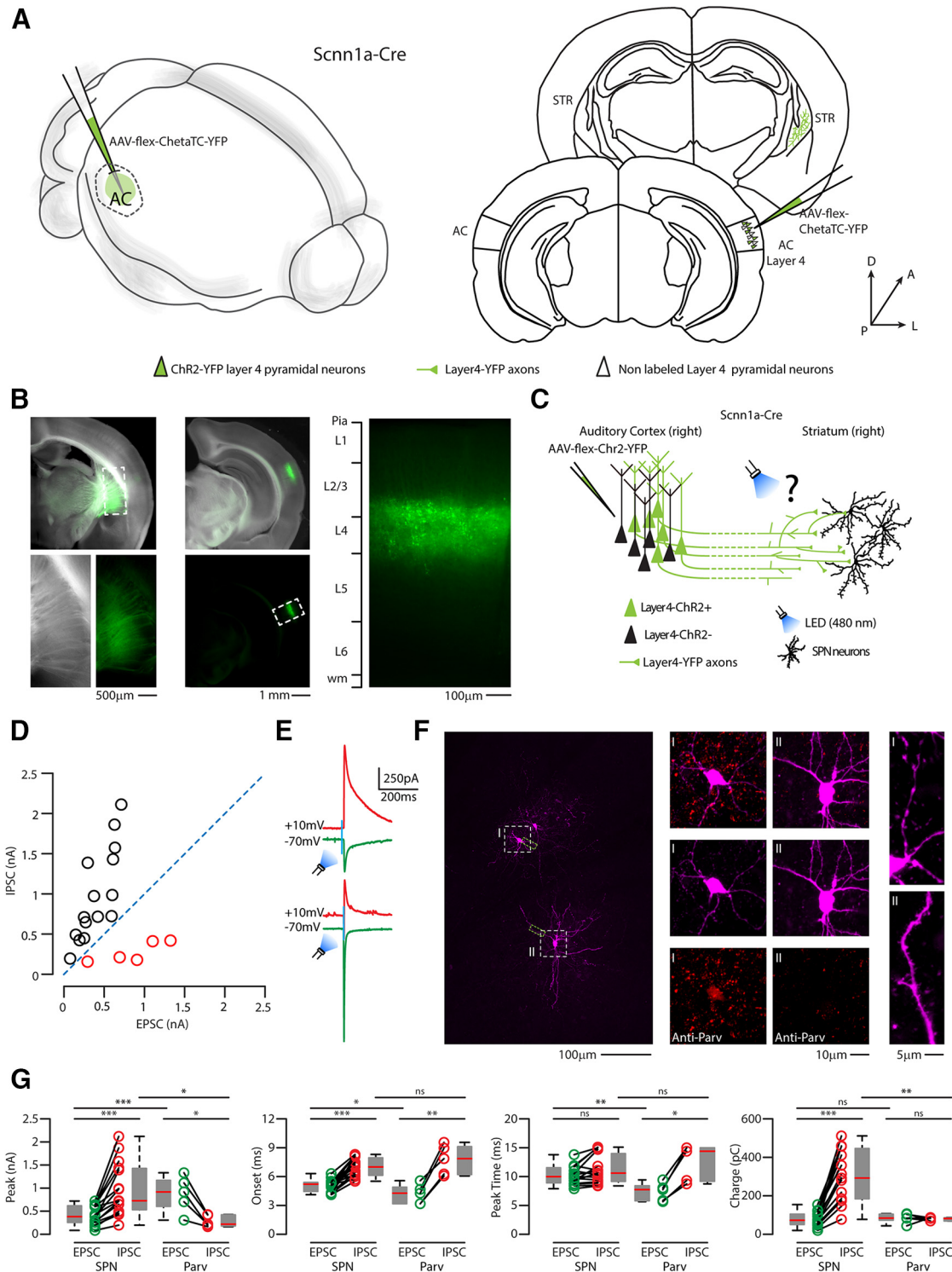


Figure 13. Photostimulation of CS-L4 projection elicits differentially excitatory and inhibitory inputs onto SPNs and intrastriatal Parv GABAergic neurons. **A**, Left, Schematic of the injection site in 3D. Right, Schematic of the Allen Brain Atlas tables and coordinates used for injections and imaging; 50 nl of AAV-flex-ChetaTC-YFP was injected in the right AC, while recordings were performed in the right striatum of Scnn1a-Cre heterozygous mice. **B**, Top left, Bright field low-magnification picture of the injection site in the striatum. Scale bar, 1 mm. Bottom left, Bright field and green fluorescence picture of higher magnification of dotted square in the top left (striatum, anatomic boundaries indicated by the dotted line). Scale bar, 500 µm. Top and bottom center, Overlap of bright field and green fluorescence picture at low magnification of the injected right AC. Scale bar, 1 mm. Left, Representative high-magnification image of YFP (green)-expressing L4 neurons in the injected AC, with layer reference on the left bar. Scale bar, 100 µm. **C**, Schematic represents the experimental paradigm: CS-L4 neurons in the AC-expressing Cheta-TC and YFP project to the right striatum, where local neurons were recorded while flashing a blue LED (480 nm). **D**, E/I graph of the 20 striatal neurons recorded. Their distribution and their E/I balance can identify two populations: one has an E/I ratio < 1 (black circles), and the other has an E/I ratio > 1 (red circles). **E**, Representative traces of EPSCs (green) and IPSCs (red) recorded in the first population (top traces) and the second one (bottom traces) while flashing the blue LED at 7 mW/mm². **F**, Left, High-magnification confocal images of confocal images of intrastriatal Parv GABAergic neurons (I) and SPN (II). Green dashed boxes represent the location of the confocal images of the dendrite for each neuron. Scale bar, 100 µm. Middle left, From top to bottom, Parv GABAergic neuron (I) immunostained with anti-Parv. Middle right, From top to bottom, SPN (II) immunostained with anti-Parv. Scale bar, 10 µm. Right top, High-magnification epifluorescence image of the dendrite of an intrastriatal Parv GABAergic neuron (I) displays the absence of spines. Right bottom, High-magnification epifluorescence image of the

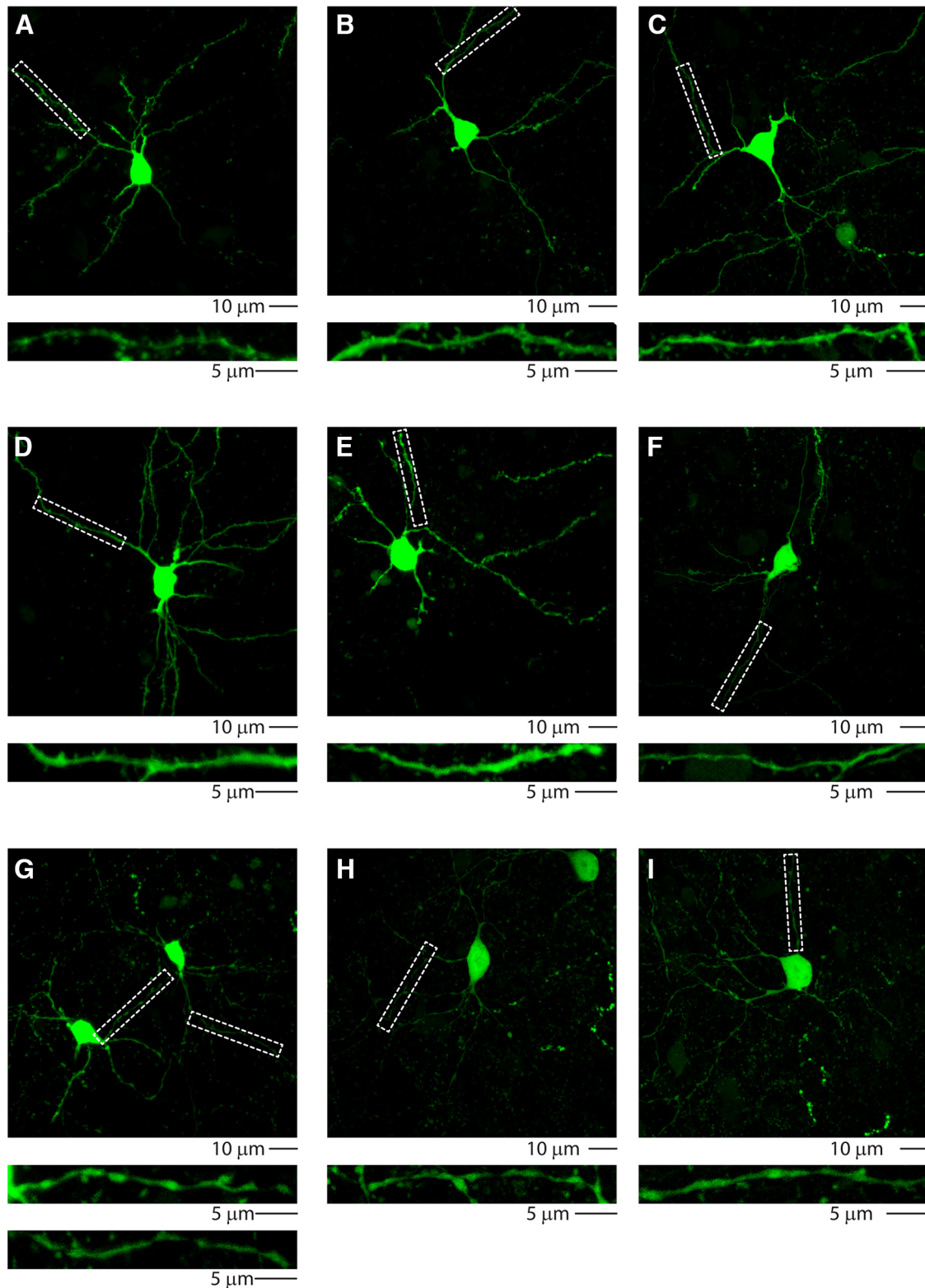


Figure 14. High-resolution images of intra-striatal Parv GABAergic neurons. High-resolution confocal images of biocytin-filled striatal neurons. Dashed lines indicate the corresponding enlargement of dendritic branches showing spiny (A–E) or smooth (F–I) morphology. Scale bars: low magnification, 10 μm; high magnification, 5 μm.

←

dendrite of an SPN (I) displays high-density dendritic spines. Scale bar, 5 μm. **G**, Quantification of EPSC (green) and IPSC (red) parameters: peak (pA), onset of response (ms), time to reach the peak (ms), and Charge (pC). Box plots represent median value and distribution. * $p < 0.05$. ** $p < 0.01$. *** $p < 0.005$.

Parv neurons supplied the main source of disynaptic inhibition on CS-L4 neurons upon thalamic stimulation.

Moreover, we performed current-clamp experiments on another set of CS-L4 neurons and determined the average number of APs on blue light only or blue and amber light combination (i.e., silencing local Parv-Halo⁺ neurons while activating

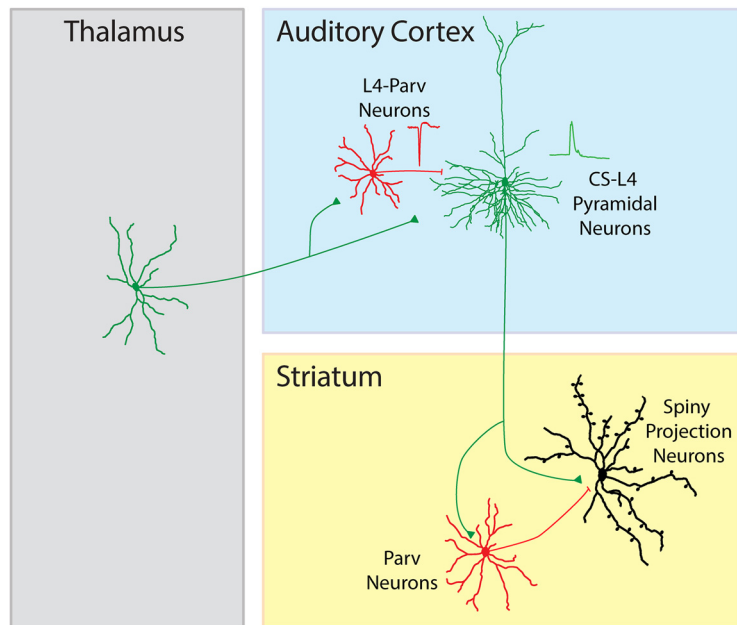


Figure 15. Summary schematic of the circuit involving novel identified CS-L4 neurons. Thalamic neurons in the MGB project to the ipsilateral AC are connected directly onto CS-L4 neurons or indirectly with a disynaptic feedforward inhibitory circuit involving local parvalbumin neurons. CS-L4 neurons project to the ipsilateral striatum, sending direct excitatory inputs onto local spiny projection neurons and local inhibitory neurons, which in turn can inhibit neighboring spiny projection neurons in a disynaptic feedforward inhibitory circuit.

thalamic axons). We found that CS-L4 neurons can initiate APs in response to thalamic axons activation only when the local Parv population is silenced (average spike probability with blue light only = $5.71 \pm 5.71\%$, average spike probability with blue and amber light = $97.14 \pm 2.86\%$, $p = 0.0006$, rank-sum test, number of neurons, $n = 7$) (Fig. 11G). Overall, our results demonstrated that local Parv neurons modulate the activity of CS-L4 neurons in a feedforward circuit under the control of direct thalamic inputs, suggesting a role for CS-L4 neurons in the direct transfer of upcoming auditory signals from the MGB to the posterior part of the dorsal striatum.

What is the cellular long-range target of CS-L4 pyramidal neurons in the posterior striatum?

To further characterize the role of CS-L4 neurons, we analyzed their output in the target region: the auditory striatum (Fig. 12). We injected the cre-dependent excitatory opsin AAV-flex-ChetaTC-YFP in the right AC of Scnn1a-Cre mice (Figs. 12 and 13A–C) and recorded E/I inputs on striatal neurons, where the terminal field of CS-L4 neurons was observed (Fig. 12). Of 20 neurons patched, we could divide them into two groups, based on their E/I profile: the first (number of neurons, $n = 15$) having an average E/I ratio of 0.04, the second (number of neurons, $n = 5$) having an average E/I ratio of 3.2 (Fig. 13D,E). Interestingly, high-resolution confocal images of the biocytin-filled neurons showed that the first group of neurons was dense in dendritic spines (indication of spiny projection neurons morphology SPNs; Fig. 14A–G), whereas the second group had smooth dendrites (Fig. 14F–I). Further characterization showed that 3 of 5 neurons in the second group also expressed parvalbumin molecular markers (Fig. 13F), suggesting that the second class comprises inhibitory local Parv neurons. EPSPs quantification in the two groups highlighted significantly higher excitatory inputs on Parv neurons (average peak SPNs = 409.26 ± 53.84 pA,

number of neurons, $n = 15$; average peak Parv = 869.28 ± 176.64 pA, number of neurons, $n = 5$; $p = 0.0032$, t test), which occur faster (average peak time SPNs = 10.21 ± 0.42 ms, number of neurons, $n = 15$; average peak time Parv = 7.3 ± 0.71 ms, number of neurons, $n = 5$; $p = 0.0025$, t test) and with shorter onset (average onset SPNs = 5.05 ± 0.17 ms, number of neurons, $n = 15$; average onset Parv = 4.2 ± 0.46 ms, number of neurons, $n = 5$; $p = 0.041$, t test). All parameters are compatible with monosynaptic inputs (Fig. 13G). On the other hand, inhibitory inputs in the two groups showed the opposite behavior, with significantly higher IPSPs on SPNs (average peak SPNs = 979.76 ± 147.36 pA, number of neurons, $n = 15$; average peak Parv = 275.62 ± 57.69 pA, number of neurons, $n = 5$; $p = 0.015$, t test), that reach the peak at the same time (average peak time SPNs = 11.25 ± 0.65 ms, number of neurons, $n = 15$; average peak time Parv = 12.48 ± 1.43 ms, number of neurons, $n = 5$; $p = 0.385$, t test) and with similar onsets (average onset SPNs = 6.95 ± 0.25 ms, number of neurons, $n = 15$; average onset Parv = 7.78 ± 0.70 ms, number of neurons, $n = 5$; $p = 0.169$, t test),

suggesting the engagement of a local inhibitory circuitry and disynaptic inhibition (Fig. 13G). This was further confirmed by abolishing IPSCs after the bath application of excitatory synaptic blockers NBQX and CPP (data not shown). This demonstrates that CS-L4 neurons target both populations, with stronger inputs on inhibitory local Parv neurons, which might be responsible for the strong inhibition of SPNs, in another feedforward inhibitory circuit.

Discussion

To date, no study has revealed a detailed understanding of the circuit mechanisms by which L4 projections modulate auditory processing in a subcortical structure, such as the striatum. A large body of evidence suggests that L4 neurons are the main thalamic recipient layer, projecting to the upper cortical L2/L3 (Huang and Winer, 2000; Sarid et al., 2007; Watkins et al., 2014). For the first time, our results demonstrate that the AC projects to the posterior part of the dorsal striatum via pyramidal neurons located in L4 (Fig. 15). In addition, expressing this quantification as the density of labeled neurons per layer, we found that L4 and L5 have the same percentage of corticostriatal neurons. We also found that the dendritic morphologies of L4 corticostriatal pyramidal neurons are different from those in other layers, which may be reflected in terms of specialized electrophysiological properties, demonstrating that L4 corticostriatal pyramidal neurons are a distinct population of corticostriatal pyramidal neurons. Although our study has demonstrated the existence of CS-L4 pyramidal neurons, additional experiments are required to determine the molecular identity of these neurons and how they differ from the one that send local and long-range inputs to other cortical targets as demonstrated by Harris et al. (2019).

Previous results have demonstrated that corticostriatal projections are primarily from two subtypes of L5 pyramidal neurons: the IT-type pyramidal neurons that project to the ipsilateral and

contralateral striatum, and the PT-type pyramidal neurons that send their axons to the downstream areas, such as the thalamus and brainstem with collaterals in the ipsilateral striatum (Landry et al., 1984; Wilson, 1987; Cowan and Wilson, 1994; Lei et al., 2004; Kress et al., 2013), while our results challenge this view, suggesting a pivotal role for CS-L4 neurons to the top-down control of the dorsal striatum as well. Moreover, we demonstrated that thalamic projections exert monosynaptic excitatory input and disinaptic inhibition that contributes via Parv-expressing GABAergic neurons to the suppression of CS-L4 neurons (thalamo→cortico(L4)→striatal) (Fig. 15). It has been demonstrated that L5 pyramidal neurons are also activated directly by the thalamus (Constantinople and Bruno, 2013; Sun et al., 2013; Egger et al., 2020). Particularly, Sun et al. (2013) demonstrated that L5 intrinsic bursting neurons (e.g., PT-type) receive direct MGB inputs, whereas regular spiking neurons (e.g., IT-type) do not. In addition, they determined that the latency of sound-evoked spike response of L5 fast spiking neurons is faster than in L5 intrinsic bursting neurons. This result led the authors to speculate that fast spiking neurons provide a potential feedforward inhibitory input onto L5 intrinsic bursting neurons of the mouse AC. However, how the thalamic inputs differentially control the output of the L4 and L5 corticofugal neurons still has to be determined. Together with L5 results, our data invited to speculate that the activity and interactions of these two layers can be modulated by different behavioral states that are driven by the comparison of sensory signals, motor actions, and/or learning.

Previous studies (Znamenskiy and Zador, 2013; Xiong et al., 2015; Ponvert and Jaramillo, 2019; Ghosh and Zador, 2021; Li et al., 2021) have characterized the neuronal mechanisms and the behavioral consequences of L5 corticostriatal neurons activity. Notably, Xiong et al. (2015) proposed a model in which the synapses between auditory cortical neurons and neurons in the striatum that can drive appropriate actions are potentiated. Recently, Li et al. (2021) showed that L5 pyramidal neurons in the mouse AC that project to the tail of the striatum respond to auditory looming stimuli invoking defense-like behaviors. Our results identified a previously unexplored CS-L4 long-range excitatory circuit underlying the control of the auditory striatum (Fig. 15). In addition, a growing body of evidence has established that the IT- and PT-type pyramidal neurons (Lei et al., 2004; Kress et al., 2013), as well as the overall excitatory inputs onto striatal neurons, can provide different excitatory inputs to the two subtype of SPNs and intrastriatal local GABAergic neurons (Kawaguchi, 1993). Notably, Johansson and Silberberg (2020) demonstrated that the ipsilateral somatosensory cortex preferentially excites SPNs and Parv-expressing neurons while the ipsilateral motor cortex targets intrastriatal GABAergic neurons more frequent than the ipsilateral somatosensory cortex. Our study similarly established that the CS-L4 pyramidal neurons differentially innervate the SPNs and intrastriatal Parv-expressing GABAergic neurons. Given that Parv-expressing spiny neurons have been described as one of the main local inhibitory inputs on SPNs (for review, see Tepper et al., 2010, 2018), we suggest that Parv-expressing intrastriatal neurons are engaging in feedforward corticostriatal disinaptic inhibitory circuits. In light of these results, we propose a new model in which CS-L4 pyramidal neurons are an important hub of the flow of thalamo-cortico-striatal information, starting in the AC with Parv-expressing GABAergic neurons controlling the integration window of CS-L4 pyramidal neurons in response to thalamic inputs and ending with a direct flow of information to the dorsal striatum. Numerous questions still need to be addressed concerning corticostriatal circuits. A

crucial line of investigation for future work is to address how different cell types located in different layers of the AC form unique connectivity patterns, potentially because of their local and long-range connectivity. Particularly, it will be important to determine how these layer-specific corticostriatal circuits may carry top-down signals conveying contextual and/or predictive information that can differentially modulate the activity of the auditory striatum. Previous cortical wiring diagrams (for review, see Douglas and Martin, 2004; Harris and Shepherd, 2015) have proposed that the activity of the L4 pyramidal neurons powerfully provides bottom-up input to the cortex. Particularly, this cortical wiring diagram was based on the seminal work of Douglas and Martin (1991) in the cat visual system that produced a model of how information flows through the cortical column. The model supports that L4 responses are dominated by feedforward thalamic input. Consequently, L4 provides the strongest ascending interlaminar connections to L2/L3. Here we propose a new wiring diagram that implements the old one, in which L4 is not only involved in the transfer of thalamic input to the upper L2/L3 but can exert a direct top-down control, bypassing intracortical processing, of subcortical structure, such as the posterior part of the dorsal striatum (thalamo→cortico(L4)→striatal) (Fig. 15), posing a new conceptual cell element (CS-L4 neurons) for experimental and theoretical work of cortical function.

References

- Agmon A, Connors BW (1991) Thalamocortical responses of mouse somatosensory (barrel) cortex in vitro. *Neuroscience* 41:365–379.
- Bertero A, Feyen PL, Zurita H, Apicella AJ (2019) A non-canonical cortico-amygdala inhibitory loop. *J Neurosci* 39:8424–8438.
- Bertero A, Zurita H, Normandin M, Apicella AJ (2020) Auditory long-range parvalbumin cortico-striatal neurons. *Front Neural Circuits* 14:45.
- Chattopadhyaya B, Di Cristo G, Higashiyama H, Knott GW, Kuhlman SJ, Welker E, Huang ZJ (2004) Experience and activity-dependent maturation of perisomatic GABAergic innervation in primary visual cortex during a postnatal critical period. *J Neurosci* 24:9598–9611.
- Chen L, Wang X, Ge S, Xiong Q (2019) Medial geniculate body and primary auditory cortex differentially contribute to striatal sound representations. *Nat Commun* 10:418.
- Constantinople CM, Bruno RM (2013) Deep cortical layers are activated directly by thalamus. *Science* 340:1591–1594.
- Cowan RL, Wilson CJ (1994) Spontaneous firing patterns and axonal projections of single corticostriatal neurons in the rat medial agranular cortex. *J Neurophysiol* 71:17–32.
- Cruikshank SJ, Rose HJ, Metherate R (2002) Auditory thalamocortical synaptic transmission in vitro. *J Neurophysiol* 87:361–384.
- Cruikshank SJ, Lewis TJ, Connors BW (2007) Synaptic basis for intense thalamocortical activation of feedforward inhibitory cells in neocortex. *Nat Neurosci* 10:462–468.
- Doig NM, Moss J, Bolam JP (2010) Cortical and thalamic innervation of direct and indirect pathway medium-sized spiny neurons in mouse striatum. *J Neurosci* 30:14610–14618.
- Douglas RJ, Martin KA (1991) A functional microcircuit for cat visual cortex. *J Physiol* 440:735–769.
- Douglas RJ, Martin KA (2004) Neuronal circuits of the neocortex. *Annu Rev Neurosci* 27:419–451.
- Egger R, Narayanan RT, Guest JM, Bast A, Udvardy D, Messori LF, Das S, de Kock CPJ, Oberlaender M (2020) Cortical output is gated by horizontally projecting neurons in the deep layers. *Neuron* 105:122–137.e8.
- Flaherty AW, Graybiel AM (1993) Two input systems for body representations in the primate striatal matrix: experimental evidence in the squirrel monkey. *J Neurosci* 13:1120–1137.
- Gabernet L, Jadhav SP, Feldman DE, Carandini M, Scanziani M (2005) Somatosensory integration controlled by dynamic thalamocortical feedforward inhibition. *Neuron* 48:315–327.
- Ghosh S, Zador AM (2021) Corticostriatal plasticity established by initial learning persists after behavioral reversal. *eNeuro* 8:ENEURO.0209-20.2021.

- Gilbert CD, Wiesel TN (1979) Morphology and intracortical projections of functionally characterized neurones in the cat visual cortex. *Nature* 280:120–125.
- Gilbert CD, Wiesel TN (1983) Functional organization of the visual cortex. *Prog Brain Res* 58:209–218.
- Graybiel AM, Grafton ST (2015) The striatum: where skills and habits meet. *Cold Spring Harb Perspect Biol* 7:a021691.
- Graybiel AM, Aosaki T, Flaherty AW, Kimura M (1994) The basal ganglia and adaptive motor control. *Science* 265:1826–1831.
- Guo Q, Wang D, He X, Feng Q, Lin R, Xu F, Fu L, Luo M (2015) Whole-brain mapping of inputs to projection neurons and cholinergic interneurons in the dorsal striatum. *PLoS One* 10:e0123381.
- Haber S (2008) Parallel and integrative processing through the Basal Ganglia reward circuit: lessons from addiction. *Biol Psychiatry* 64:173–174.
- Harris KD, Shepherd GM (2015) The neocortical circuit: themes and variations. *Nat Neurosci* 18:170–181.
- Harris JA, Mihalas S, Hirokawa KE, Whitesell JD, Choi H, Bernard A, Bohn P, Caldejon S, Casal L, Cho A, Feiner A, Feng D, Gaudreault N, Gerfen CR, Graddis N, Groblewski PA, Henry AM, Ho A, Howard R, Knox JE, et al. (2019) Hierarchical organization of cortical and thalamic connectivity. *Nature* 575:195–202.
- Huang CL, Winer JA (2000) Auditory thalamocortical projections in the cat: laminar and areal patterns of input. *J Comp Neurol* 427:302–331.
- Huggenberger S, Vater M, Deisz RA (2009) Interlaminar differences of intrinsic properties of pyramidal neurons in the auditory cortex of mice. *Cereb Cortex* 19:1008–1018.
- Ji XY, Zingg B, Mesik L, Xiao Z, Zhang LI, Tao HW (2016) Thalamocortical innervation pattern in mouse auditory and visual cortex: laminar and cell-type specificity. *Cereb Cortex* 26:2612–2625.
- Johansson Y, Silberberg G (2020) The functional organization of cortical and thalamic inputs onto five types of striatal neurons is determined by source and target cell identities. *Cell Rep* 30:1178–11943.e1173.
- Kawaguchi Y (1993) Physiological, morphological, and histochemical characterization of three classes of interneurons in rat neostriatum. *J Neurosci* 13:4908–4923.
- Kress GJ, Yamawaki N, Wokosin DL, Wickersham IR, Shepherd GM, Surmeier DJ (2013) Convergent cortical innervation of striatal projection neurons. *Nat Neurosci* 16:665–667.
- Landry P, Wilson CJ, Kitai ST (1984) Morphological and electrophysiological characteristics of pyramidal tract neurons in the rat. *Exp Brain Res* 57:177–190.
- Lee CC, Sherman SM (2008) Synaptic properties of thalamic and intracortical inputs to layer 4 of the first- and higher-order cortical areas in the auditory and somatosensory systems. *J Neurophysiol* 100:317–326.
- Lee CC, Winer JA (2008) Connections of cat auditory cortex: I. Thalamocortical system. *J Comp Neurol* 507:1879–1900.
- Lei W, Jiao Y, Del Mar N, Reiner A (2004) Evidence for differential cortical input to direct pathway versus indirect pathway striatal projection neurons in rats. *J Neurosci* 24:8289–8299.
- Li Z, Wei JX, Zhang GW, Huang JJ, Zingg B, Wang X, Tao HW, Zhang LI (2021) Corticostriatal control of defense behavior in mice induced by auditory looming cues. *Nat Commun* 12:1040.
- Linden JF, Schreiner CE (2003) Columnar transformations in auditory cortex? A comparison to visual and somatosensory cortices. *Cereb Cortex* 13:83–89.
- Metherate R, Aramakis VB (1999) Intrinsic electrophysiology of neurons in thalamorecipient layers of developing rat auditory cortex. *Brain Res Dev Brain Res* 115:131–144.
- Mitani A, Shimokouchi M (1985) Neuronal connections in the primary auditory cortex: an electrophysiological study in the cat. *J Comp Neurol* 235:417–429.
- Mitani A, Shimokouchi M, Itoh K, Nomura S, Kudo M, Mizuno N (1985) Morphology and laminar organization of electrophysiologically identified neurons in the primary auditory cortex in the cat. *J Comp Neurol* 235:430–447.
- Park Y, Geffen MN (2020) A circuit model of auditory cortex. *PLoS Comput Biol* 16:e1008016.
- Ponvert ND, Jaramillo S (2019) Auditory thalamostriatal and corticostriatal pathways convey complementary information about sound features. *J Neurosci* 39:271–280.
- Rock C, Zurita H, Wilson C, Apicella AJ (2016) An inhibitory corticostriatal pathway. *Elife* 5:e15890.
- Rock C, Zurita H, Leiby S, Wilson CJ, Apicella AJ (2017) Cortical circuits of callosal GABAergic neurons. *Cereb Cortex* 28:1154–1167.
- Rose HJ, Metherate R (2005) Auditory thalamocortical transmission is reliable and temporally precise. *J Neurophysiol* 94:2019–2030.
- Sarid L, Bruno R, Sakmann B, Segev I, Feldmeyer D (2007) Modeling a layer 4-to-layer 2/3 module of a single column in rat neocortex: interweaving in vitro and in vivo experimental observations. *Proc Natl Acad Sci USA* 104:16353–16358.
- Schiff ML, Reyes AD (2012) Characterization of thalamocortical responses of regular-spiking and fast spiking neurons of the mouse auditory cortex in vitro and in silico. *J Neurophysiol* 107:1476–1488.
- Schultz W, Dayan P, Montague PR (1997) A neural substrate of prediction and reward. *Science* 275:1593–1599.
- Schindelin J, Arganda-Carreras I, Frise E, Kaynig V, Longair M, Pietzsch T, Preibisch S, Rueden C, Saalfeld S, Schmid B, Tinevez JY, White DJ, Hartenstein V, Eliceiri K, Tomancak P, Cardona A (2012) Fiji: an open-source platform for biological-image analysis. *Nat Methods* 9:676–682.
- Shepherd GM (2013) Corticostriatal connectivity and its role in disease. *Nat Rev Neurosci* 14:278–291.
- Sun YJ, Kim YJ, Ibrahim LA, Tao HW, Zhang LI (2013) Synaptic mechanisms underlying functional dichotomy between intrinsic-bursting and regular-spiking neurons in auditory cortical layer 5. *J Neurosci* 33:5326–5339.
- Suter BA, O'Connor T, Iyer V, Petreanu LT, Hooks BM, Kiritani T, Svoboda K, Shepherd GM (2010) Ephus: multipurpose data acquisition software for neuroscience experiments. *Front Neural Circuits* 4:100.
- Tepper JM, Abercrombie ED, Bolam JP (2007) Basal ganglia macrocircuits. *Prog Brain Res* 160:3–7.
- Tepper JM, Tecuapetla F, Koós T, Ibáñez-Sandoval O (2010) Heterogeneity and diversity of striatal GABAergic interneurons. *Front Neuroanat* 4:150.
- Tepper JM, Koós T, Ibanez-Sandoval O, Tecuapetla F, Faust TW, Assous M (2018) Heterogeneity and diversity of striatal GABAergic interneurons: update 2018. *Front Neuroanat* 12:91.
- Vasquez-Lopez SA, Weissenberger Y, Lohse M, Keating P, King AJ, Dahmen JC (2017) Thalamic input to auditory cortex is locally heterogeneous but globally tonotopic. *Elife* 6:e25141.
- Verbny YI, Erdelyi F, Szabo G, Banks MI (2006) Properties of a population of GABAergic cells in murine auditory cortex weakly excited by thalamic stimulation. *J Neurophysiol* 96:3194–3208.
- Watkins PV, Kao JP, Kanold PO (2014) Spatial pattern of intra-laminar connectivity in supragranular mouse auditory cortex. *Front Neural Circuits* 8:15.
- Wilson CJ (1987) Morphology and synaptic connections of crossed corticostriatal neurons in the rat. *J Comp Neurol* 263:567–580.
- Winer JA (1984) Anatomy of layer IV in cat primary auditory cortex (AI). *J Comp Neurol* 224:535–567.
- Winkowski DE, Kanold PO (2013) Laminar transformation of frequency organization in auditory cortex. *J Neurosci* 33:1498–1508.
- Xiong Q, Znamenskiy P, Zador AM (2015) Selective corticostriatal plasticity during acquisition of an auditory discrimination task. *Nature* 521:348–351.
- Zhou M, Liang F, Xiong XR, Li L, Li H, Xiao Z, Tao HW, Zhang LI (2014) Scaling down of balanced excitation and inhibition by active behavioral states in auditory cortex. *Nat Neurosci* 17:841–850.
- Znamenskiy P, Zador AM (2013) Corticostriatal neurons in auditory cortex drive decisions during auditory discrimination. *Nature* 497:482–485.
- Zurita H, Feyen PL, Apicella AJ (2018a) Layer 5 callosal parvalbumin-expressing neurons: a distinct functional group of GABAergic neurons. *Front Cell Neurosci* 12:53.
- Zurita H, Rock C, Perkins J, Apicella AJ (2018b) A layer-specific corticofugal input to the mouse superior colliculus. *Cereb Cortex* 28:2817–2833.